New technique to diagnose the geomagnetic field based on the single circular current loop model

Zhaojin Rong[1], Yong Wei[2], Masatoshi Yamauchi[3], Wenyao Xu[2], Dali Kong[4], Jun Cui[5], Chao Shen[6], Rixiang Zhu[2], Weixing Wan[7], Jun Zhong[2], and Lihui Chai[2]

[1]Key Laboratory of Earth and Planetary Physics, Institute of Geology and Geophysics, Chinese Academy of Sciences
[2]Institute of Geology and Geophysics, Chinese Academy of Sciences
[3]Swedish Institute of Space Physics
[4]Shanghai Astronomical Observatory
[5]Sun Yat-sen University
[6]Harbin Institute of Technology
[7]Institute of Geology and Geophysics,Chinese Academy of Sciences

November 21, 2022

Abstract

A quick and effective technique is developed to diagnose the geomagnetic dipole field based on an unstrained single circular current loop model. In comparsion with previous studies, this technique is able to separate and solve the loop parameters successively. With this technique, one can search the optimum full loop parameters quickly, including the location of loop center, the loop orientation, the loop radius, and the electric current carried by the loop, which can roughly indicate the locations, sizes, orientations of the interior current sources. The technique tests and applications demonstrate that this technique is effective and applicable. This technique could be applied widely in the fields of geomagnetism, planetary magnetism and palaeomagnetism. The further applications and constrains are discussed and cautioned.

New technique to diagnose the geomagnetic field based on the single circular current loop model

Z. J. Rong[1, 2, 3], Y. Wei[1, 2, 3], M. Yamauchi[4], W. Y. Xu[1], D. L. Kong[5], J. Cui[6], C. Shen[7], R. X. Zhu[1, 2], W. X. Wan[1, 2, 3], J. Zhong[1, 2, 3], L. H. Chai[1, 2, 3]

[1]Key Laboratory of Earth and Planetary Physics, Institute of Geology and Geophysics, Chinese Academy of Sciences, Beijing 100029, China

[2]College of Earth and Planetary Sciences, University of Chinese Academy of Sciences, Beijing, China

[3]Beijing National Observatory of Space Environment, Institute of Geology and Geophysics, Chinese Academy of Sciences, Beijing, China

[4]Swedish Institute of Space Physics, Kiruna, Sweden

[5]Shanghai Astronomical Observatory, Chinese Academy of Sciences, Shanghai 200030, China

[6]School of Atmospheric Sciences, Sun Yat-Sen University, Zhuhai 519082, China.

[7]Harbin Institute of Technology, Shenzhen, China,

Correspondence to: rongzhaojin@mail.iggcas.ac.cn

Keywords: Geomagnetic field, Dipole field, Spherical harmonic analysis, Current loop, Dynamo currents, Planetary magnetic field

Abstract

A quick and effective technique is developed to diagnose the geomagnetic dipole field based on an unstrained single circular current loop model. In comparsion with previous studies, this technique is able to separate and solve the loop parameters successively. With this technique, one can search the optimum full loop parameters quickly, including the location of loop center, the loop orientation, the loop radius, and the electric current carried by the loop, which can roughly indicate the locations, sizes, orientations of the interior current sources. The technique tests and applications demonstrate that this technique is effective and applicable. This technique could be applied widely in the fields of geomagnetism, planetary magnetism and palaeomagnetism. The further applications and constrains are discussed and cautioned.

1. Introduction

The most frequently used method to analyze geomagnetic field is the spherical harmonic analysis (SHA), which is based on the solution of the Laplace equation with assumption of no electric current in the concerned domain, that is $\nabla^2 U = 0$ and $\mathbf{B} = -\nabla U$,where U is the magnetic poential and **B** is the magnetic vector. With SHA, the solution of U can be expanded as the sum of Associated Legendre polynomials,

$$U = r_0 \sum_{n=1}^{\infty} \sum_{m=0}^{n} P_n^m(\cos\theta) \left[\left(\frac{r_0}{r}\right)^{n+1} \left(g_n^m \cos m\lambda + h_n^m \sin m\lambda\right) + \left(\frac{r_0}{r}\right)^{-n} \left(A_n^m \cos m\lambda + B_n^m \sin m\lambda\right) \right]$$

, where r_0, r, θ, λ are the Earth's radius, radial distance, geocentric colatitude, and the longitude of a given location, respectively, P_n^m are the associated Legendre polynomials, g_n^m and h_n^m are the Gauss coefficients are related with the internal magnetic sources, while A_n^m and B_n^m are the coefficients related with the external sources [Chapman & Bartels, 1940; Merrill, McElhinny, & McFadden, 1996]. The internal dipole moment **M** is defined using the first three internal coefficients g_1^0, g_1^1 and h_1^1, that is, $M = \frac{\mu_0}{4\pi r_0^3}\sqrt{\left(g_1^0\right)^2 + \left(g_1^1\right)^2 + \left(h_1^1\right)^2}$, where μ_0 is the permeability in vacuum [e.g. Amit and Olson, 2008]. The other Gauss coefficients of the internal sources represent the multipole (quadrupole, octupole, etc.) components. Since the dipole component dominates the field, the geomagnetic field at Earth's surface can be well approximated as a geocentered dipole field model. To make the dipole model more accurate, the eccentric dipole approximation was also made in some studies[James & Winch, 1967; Cain, Schmitz, & Kluth, 1985; Fraser-Smith, 1987].

It has to be reminded that SHA has some assumptions and constraints though it is widely used: 1. The magnetic field in concerned spatial region should satisfy potential field, but the assumption would propablly fail when electric currents present in concerned region. 2. The Gauss coefficients cannot indicate the “real” magnetic sources directly. For example, an offset of a dipole center is mathematically indistinguishable from a dipole plus a series of higher multipole field at Earth’s center [see page 42 of Merrill, McElhinny, & McFadden, 1996].

Alternatively, some physical models with idealized assumptions were developed to fit the geomagnetic field. In almost all these attempts, multiple magnetic dipoles were used to represent the sources of magnetic field (e.g. one centered axial dipole with several eccentric radial dipoles [McNish, 1940;Alldredge and Hurwitz,1964;

Alldredge and Stearns,1969]; two horizontal dipoles [Lyakhov, 1960]; one to six unconstrained dipoles [Bochev,1975]; 93 dipoles constrained at the core-mantle boundaries [Mayhew and Estes, 1983]).

The magnetic dipole is only a special case of a circular current loop whose radius is zero, and models of single loop and also multiple loops have privously been proposed as more physical representations of geomagnetic field [e.g. Zidarov and Petrova, 1974; Peddie, 1979; Zidarov, 1985; Demina and Farafonova, 2016]. It is well-known that seven free parameters are required to characterize a circular current loop, that is, the location of loop center (three parameters), the orientation of loop axis (two parameters), the loop radius (one parameters), and the electric current (one parameters) carried by the loop. Those parameters are meaningful to indicate the equvalient geometric characteristics of interior currents, though the actual currents pattern could be far more complicated than a circular current loop.

Problem is that the simutaneous least-square fitting of these loop parameters would result in multiple solutions of parameter sets. To search the best set of parameters from the multiple solutions is not an easy task, even for a single current loop model. Because the optimum fitting is strongly dependent on the initial input parameters, no general technique exists for determining whether a particular minimum error corresponds to the best solution. The more loops involved, more parameters are required, and the worse the calculation becomes unless additional constrains and assumptions are made [Peddie, 1979; Zidarov, 1985; Alldredge, 1987; Demina and Farafonova, 2016]. Peddie [1979] tried to avoid this problem by making 20 preliminary computer runs using random initial parameters for his loop models. Zidarov [1985] chose a suitable initial “point” of loop parameters to iterate the calculation in his multiple loops model. In the study of Alldredge [1987], the initial values were chosen by referring to results obtained by Benton and Alldredge [1987]. Demina and Farafonova [2016] selected 23 starting points to invert the seven parameters of single current loop.

Besides Earth, many planets in the solar system are found to possess an intrinsic global dipole-dominated field, e.g. Mercury, Jupiter, Saturn, Uranus, and Neptune. In the past decades, the measurements of spacecaft orbiting these planets accumlated amounts of planetary magnetic field data. Since no magnetic observatories avaliable on the planetary surface, the sampled field data by spacecraft usually couldn’t be the ideal potential field due to the presence of space currents; this makes it difficult to apply SHA to the non-potential field sampled by spacecraft, although planetary magnetic field models based on SHA are already existent [e.g. Connerney, 1993; Anderson et al., 2011; Schubert and Soderlund, 2011, and references therein]. Taking the magnetic field measurement of MErcury Surface, Space ENvironment, GEochemistry, and Ranging (MESSENGER) on Mercury as example, Johnson et al. [2012] argued that the fundamental assumption of a current-free region of SHA is violated, and the orbit geometry of spacecraft can result in covariance among the lowest degree and order internal and external fields.

Therefore, to diagnose the planetary dipole-dominated field generally with the magnetometer data of spacercraft, and to avoid the dilema of fitting the full parameters simultaneously, we are motivated to develop a new technique to invert the parameters of an unstrained single circular loop based on spacecraft's measurements along arbitrary trajectory. This technique could be applied widely not only to the measurements of geomagnetic observatories, but also the spacecraft's magnetometer data of planetary dipole-dominated field, to probe the complicated interior current sources [Constable and Constable, 2004]. In contrast to the fitting method, this inversion technique should be able to separate and solve the loop parameters successively without requirement of inputting the initial values.

To guarantee the inversion validity, the used field data is required to be unaffected significantly by the external sources, or the external field can be well evaluated and substracted during the data-preprocesses.

In this paper, we first present the technique algorithm in Section 2. To show the technique validity, the applications to the sampled data from International Geomagnetic Reference Field (IGRF) model and from geomagnetic observatories are conducted in Section 3 and Section 4 respectively. We make comparsions with previous studies of the loop models in Section 5. We discuss the prospect of further applications in Section 6. Finally, we discuss the physical interpretations of inverted loop parameters in Section 7, and summarize this study in Section 8.

2. Methodology

Assuming a single circular current loop, we here describe the new technique to separate the full loop parameters from the sampled magnetic field dataset by spacecraft or geomagnetic observatories. The sampled field data is assumed to be an ideal field dataset from purely internal sources; otherwise the inferred parameters would contain the contamination of external field.

2.1 The setup of coordinates

Since the geomagnetic field is corotated with Earth's rotation, this technique is convenient to be studied in the geocentric coordinates where the origin point is at Earth's center, the x-axis points towards the intersection of the equator and the Greenwich meridian, z-axis parallel to the Earth's rotation axis (positive to the north) , and y-axis completes a right-handed orthongonal set.

As shown in Figure 1, the source of the magnetic field is assumed to be a circular current loop with radius *a* carrying electric current *I*. In the orthogonal geocentric coordinates {x,y,z}, the loop center is located at $\mathbf{r}_0\left(x_0\hat{\mathbf{x}}, y_0\hat{\mathbf{y}}, z_0\hat{\mathbf{z}}\right)$, where $\hat{\mathbf{x}}, \hat{\mathbf{y}}$, and $\hat{\mathbf{z}}$ are the unit vectors along the positive direction of x-axis, y-axis, and z-axis, respectively. The loop axis-orientation is $\hat{\mathbf{M}}\left(\sin\theta_0\cos\varphi_0\hat{\mathbf{x}}, \sin\theta_0\sin\varphi_0\hat{\mathbf{y}}, \cos\theta_0\hat{\mathbf{z}}\right)$, which is the unit direction of the dipole moment $\mathbf{M}$ ($\hat{\mathbf{M}}=\mathbf{M}/\left|\mathbf{M}\right|$), where $\theta_0(0°\le\theta_0\le 180°)$ and $\varphi_0(0°\le\varphi_0\le 360°)$ are the polar angle (colatitude) and azimuthal angle of $\hat{\mathbf{M}}$, respectively. $\hat{\mathbf{M}}$ is assumed to be fixed within the period of sampling data. At the time of t_i, a spacecraft is located at $\mathbf{r}_i\left(x_i\hat{\mathbf{x}}, y_i\hat{\mathbf{y}}, z_i\hat{\mathbf{z}}\right)$ along the trajectory, and the recorded magnetic field vector is $\mathbf{B}_i$. The position vector of the spacecraft relative to the loop center is $\mathbf{R}_i = \mathbf{r}_i - \mathbf{r}_0$.

Our task is to use the sampled magnetic field $\mathbf{B}_i$, along the trajectory $\mathbf{r}_i$, by spacecraft, to estimate the unknown parameters *a*, *I*, $\mathbf{r}_0$, and $\hat{\mathbf{M}}$ of the current loop.

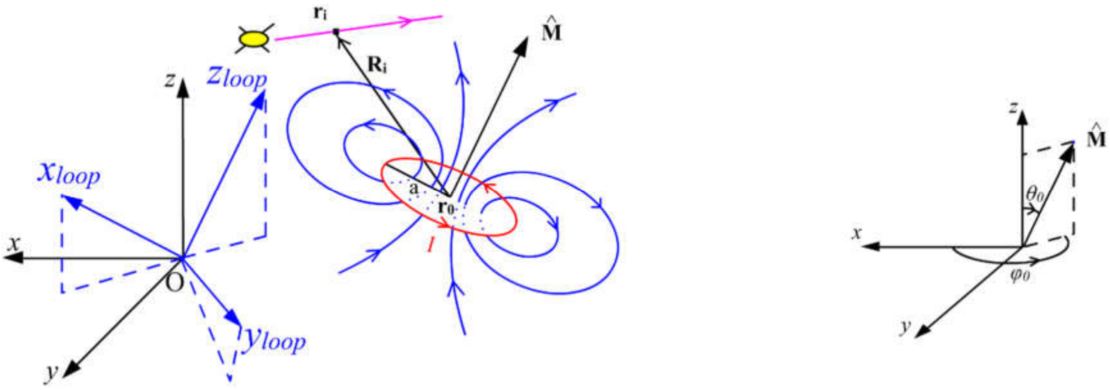

Figure 1. The location of current loop in the geocentric coordinates{x,y,z}. The circular loop with radius a and the carried electric current I is marked as a red circle whose axis orientation is along $\hat{\mathbf{M}}$. *The loop center is at* $\mathbf{r}_0$. *The loop plane and its axis orientation constitute a geocentered loop coordinates* $\{x_{loop}, y_{loop}, z_{loop}\}$: *the loop plane is in the plane constituted by* x_{loop} *and* y_{loop}, *the axis orientation is along the direction of* z_{loop}. *The origin is at geocenter* ***O*** *instead of loop center. The trajectory of spacecraft is labelled as a magenta line.*

In the frame of geocentric coordinates, it is convenient to construct a geocentric loop coordinates for the field. The loop coordinates are defined as:

$$\begin{cases} \hat{\mathbf{z}}_{loop} = \hat{\mathbf{M}} \\ \hat{\mathbf{y}}_{loop} = \dfrac{\hat{\mathbf{z}}_{loop} \times \hat{\mathbf{x}}}{\left|\hat{\mathbf{z}}_{loop} \times \hat{\mathbf{x}}\right|} \\ \hat{\mathbf{x}}_{loop} = \hat{\mathbf{y}}_{loop} \times \hat{\mathbf{z}}_{loop} \end{cases}, \tag{1}$$

the origin point is at Earth's center **O**. The loop plane is in the plane constituted by $\hat{\mathbf{x}}_{loop}$ and $\hat{\mathbf{y}}_{loop}$, and the loop center $\mathbf{r}_0$ is at $\left(x_0^{'}\hat{\mathbf{x}}_{loop}, y_0^{'}\hat{\mathbf{y}}_{loop}, z_0^{'}\hat{\mathbf{z}}_{loop}\right)$ in this coordinates. Note that, the superscript "$'$ " , unless otherwise stated, is the vector component that is expressed in the geocentric loop coordinates.

2.2. The loop axis and the loop center

Since the ideal loop field has no azimuthal component, the field lines that are diverged from or converged into the loop center, should be radially orientated in the equatorial plane of the loop coordinates. Therefore, the loop axis orientation should be the direction along which the projected field lines are mostly radially orientated. Therefore, we now consider 2D projection on the equatrial plane as shown in Figure 2. At the time t_i , the projected spacecraft location is $\mathbf{r}_{ip}\left(x_i^{'}\hat{\mathbf{x}}_{loop}, y_i^{'}\hat{\mathbf{y}}_{loop}\right)$, and the projected field orientation is $\mathbf{b}_{ip}\left(b_{xi}^{'}\hat{\mathbf{x}}_{loop}, b_{yi}^{'}\hat{\mathbf{y}}_{loop}\right)$, where, $x_i^{'} = \mathbf{r}_i \cdot \hat{\mathbf{x}}_{loop}$, $y_i^{'} = \mathbf{r}_i \cdot \hat{\mathbf{y}}_{loop}$, $b_{xi}^{'} = \dfrac{\mathbf{B}_i \cdot \hat{\mathbf{x}}_{loop}}{|\mathbf{B}_i|}$, and $b_{yi}^{'} = \dfrac{\mathbf{B}_i \cdot \hat{\mathbf{y}}_{loop}}{|\mathbf{B}_i|}$.

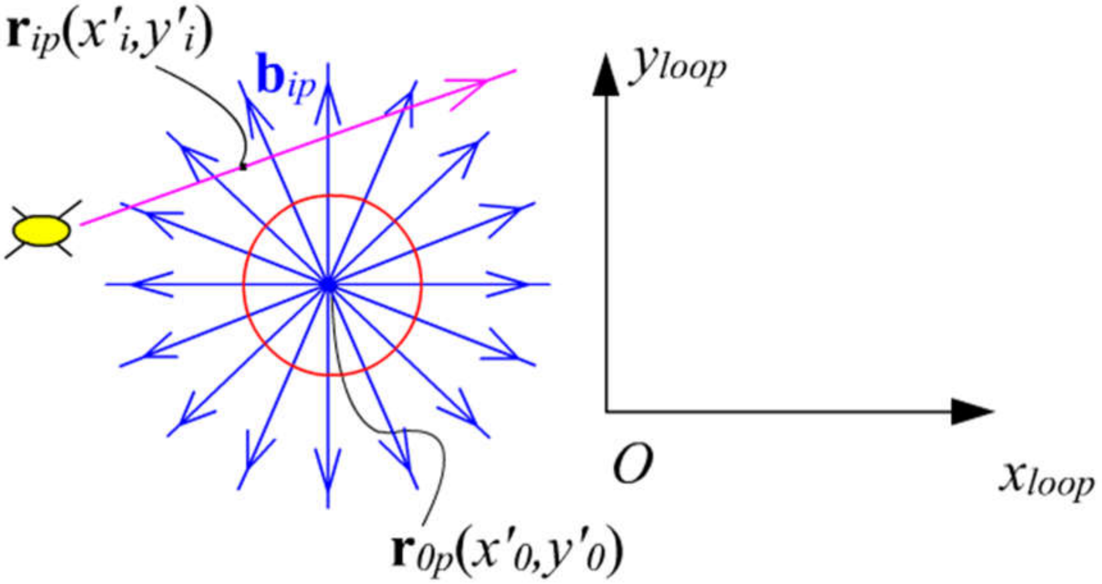

Figure 2. The projection of sampled magnetic field vectors on the equtorial plane of loop coordinates. At time t_i the spacecraft is located at the point $\mathbf{r}_{ip}\left(x_i^{'}\hat{\mathbf{x}}_{loop}, y_i^{'}\hat{\mathbf{y}}_{loop}\right)$ with the sampled magnetic vector $\mathbf{b}_{ip}$. The magneta line with arrow represents the projected trajectory of the spacecraft. The blue lines with arrow represent the projected directions of field lines. The red circle represents the current loop. The loop center is located at $\mathbf{r}_{0p}\left(x_0^{'}\hat{\mathbf{x}}_{loop}, y_0^{'}\hat{\mathbf{y}}_{loop}\right)$.

Given an arbitrary axis orientation $\hat{\mathbf{M}}$, one can setup a corresponding loop coordinates according to Eq.(1). The loop center is at $\mathbf{r}_{0p}\left(x_0^{'}\hat{\mathbf{x}}_{loop}, y_0^{'}\hat{\mathbf{y}}_{loop}\right)$. As a result, the angle α_i between $\mathbf{b}_{ip}$ and the radial orientation $\mathbf{r}_{ip} - \mathbf{r}_{0p}$ can be derived as

$$\sin\alpha_i = \frac{(\mathbf{r}_{ip}-\mathbf{r}_{0p})\times\mathbf{b}_{ip}}{|\mathbf{r}_{ip}-\mathbf{r}_{0p}||\mathbf{b}_{ip}|} = \frac{(x_i^{'}-x_0^{'})b_{yi}^{'}-(y_i^{'}-y_0^{'})b_{xi}^{'}}{\sqrt{b_{xi}^{'\,2}+b_{yi}^{'\,2}}\sqrt{(x_i^{'}-x_0^{'})^2+(y_i^{'}-y_0^{'})^2}} \tag{2}$$

If the projected field lines are perfectly radially orientated, $\mathbf{b}_{ip}$ should be parallel or anti-parallel to $\mathbf{r}_{ip}-\mathbf{r}_{0p}$, and $\sin\alpha_i$ should be equal to zero.

Thus one can construct a residue equation as

$$\alpha = \frac{1}{N}\sum_i a\sin(|\sin\alpha_i|) \tag{3}$$

Where, N is total number of the sampled data points, and i=1, 2, …N. Because $x_i^{'}$, $y_i^{'}$, $b_{xi}^{'}$, and $b_{yi}^{'}$ are denpendent on $\hat{\mathbf{M}}(\theta_0, \varphi_0)$, α is actualy the function of four parameters which depends on the axis orientation $\hat{\mathbf{M}}(\theta_0, \varphi_0)$ and the loop center $\mathbf{r}_{0p}$ $(x_0^{'}, y_0^{'})$. In other words, the optimum of $\hat{\mathbf{M}}$ and $\mathbf{r}_{0p}$ should make α reach the global minimum in the parameter space.

To search the global minimum of α quickly, we further separate $\hat{\mathbf{M}}$ and $\mathbf{r}_{0p}$ to simplify the calculation of Eq.(3).

In the equatorial plane of loop coordinates, at time t_i, the linear equation for the field line crossing the point $\mathbf{r}_{ip}\left(x_i^{'}\hat{\mathbf{x}}_{loop}, y_i^{'}\hat{\mathbf{y}}_{loop}\right)$ could be written as

$$b_{yi}^{'}\left(x-x_i^{'}\right)-b_{xi}^{'}\left(y-y_i^{'}\right)=0, \tag{4}$$

when the recorded field vector is $\mathbf{b}_{ip}\left(b_{xi}^{'}\hat{\mathbf{x}}_{loop}, b_{yi}^{'}\hat{\mathbf{y}}_{loop}\right)$.

For the ideal loop field, all the lines shoud ideally intersect at the loop center $\mathbf{r}_{0p}\left(x_0^{'}\hat{\mathbf{x}}_{dipole}, y_0^{'}\hat{\mathbf{y}}_{dipole}\right)$ in the equtorial plane. Thus, for any field line, we have

$$b_{yi}^{'}\left(x_0^{'}-x_i^{'}\right)-b_{xi}^{'}\left(y_0^{'}-y_i^{'}\right)=0. \tag{5}$$

Considering the similar formula of Eq. (5) for the other satellite positions, we could generally write Eq. (5) as the form $AX=Y$, where,

$$A = \begin{pmatrix} b'_{y1} & -b'_{x1} \\ b'_{y2} & -b'_{x2} \\ \cdots & \cdots \\ b'_{yN} & -b'_{xN} \end{pmatrix}, X = \begin{pmatrix} x'_0 \\ y'_0 \end{pmatrix}, Y = \begin{pmatrix} x'_1 b'_{y1} - y'_1 b'_{x1} \\ x'_2 b'_{y2} - y'_2 b'_{x2} \\ \cdots \\ x'_N b'_{yN} - y'_N b'_{xN} \end{pmatrix} \tag{6}$$

The optimum solution of X is

$$X = \left(A^T A\right)^{-1} A^T Y \tag{7}$$

, where $A^T A$ is a 2×2 matrix.

Obviously, the optimum X is a function of the axis orientation $\hat{\mathbf{M}}(\theta_0, \varphi_0)$. Substituting X into Eq. (3), one can obtain the minimum of α, α_{min}, for a given axis orientation. In other words, α_{min} is a function of axis orientation $\hat{\mathbf{M}}(\theta_0, \varphi_0)$. Thus, one can search the global minimum of α_{min} quickly in the 2-D map constituted by θ_0 and φ_0 to find the optimum axis orientation $\hat{\mathbf{M}}(\theta_0, \varphi_0)$ as well as the correspnding loop center $\mathbf{r}_{0p}\left(x'_0 \hat{\mathbf{x}}_{loop}, y'_0 \hat{\mathbf{y}}_{loop}\right)$.

Since both the parallel and anti-parallel directions of $\hat{\mathbf{M}}$ are valid axis orientations, we choose the one as the final $\hat{\mathbf{M}}$ along which the loop field satisfies the right-handed system. Taking the geomagnetic field as example, the polar angle of $\hat{\mathbf{M}}$ should be $\theta_0 \geq 90°$, because the field diverges in southern hemisphere.

2.3.The loop radius

Once the axis orientation is determined, we can also solve the loop radius.

The ideal magnetic field of a circular current loop is analytically calculated in textbooks [e.g. Knoepfel, 2000]. At time t_i along the trajectory, the analytic radial and axial field components are written respectively as follows:

$$\tilde{B}_{ir} = \frac{\mu_0 I}{4\pi} \frac{2\cos\theta_i}{\sin\theta_i \sqrt{a^2 + R_i^2 + 2aR_i \sin\theta_i}} \left[\frac{a^2 + R_i^2}{a^2 + R_i^2 - 2aR_i \sin\theta_i} E - K \right], \tag{8}$$

$$\tilde{B}_{iz}=\frac{\mu_0 I}{4\pi}\frac{2}{\sqrt{a^2+R_i^2+2aR_i\sin\theta_i}}\left[\frac{a^2-R_i^2}{a^2+R_i^2-2aR_i\sin\theta_i}E+K\right] \tag{9}$$

where, I is the electric current, a is the loop radius, R_i is the radial distance of spacecraft to the loop center, $\theta_i (0° \le \theta_i \le 180°)$ is the polar angle of $\mathbf{R}_i$ deviated from the loop axis orientation $\hat{\mathbf{M}}$, and the overhead "$\sim$" means that the field components are expressed in the loop-centered cylindrical coordinates (it is the same with the loop coordinates as defined in Eq.(1) but the origin becomes the loop center). E and K are the elliptical functions, that is,

$$\begin{cases} K=\int_0^{\pi/2}\frac{dx}{\sqrt{1-k^2\sin^2 x}}=\frac{\pi}{2}\left[1+\left(\frac{1}{2}\right)^2 k^2+\left(\frac{1\cdot 3}{2\cdot 4}\right)^2 k^4+\left(\frac{1\cdot 3\cdot 5}{2\cdot 4\cdot 6}\right)^2 k^6+...\right] \\ E=\int_0^{\pi/2}\sqrt{1-k^2\sin^2 x}dx=\frac{\pi}{2}\left[1-\left(\frac{1}{2}\right)^2 k^2+\left(\frac{1\cdot 3}{2\cdot 4}\right)^2 \frac{k^4}{3}+\left(\frac{1\cdot 3\cdot 5}{2\cdot 4\cdot 6}\right)^2 \frac{k^6}{5}+...\right] \\ k^2=\frac{4aR_i\sin\theta_i}{a^2+R_i^2+2aR_i\sin\theta_i} \end{cases} \tag{10}$$

In Eqs.(8-10), the radial distance R_i and the polar angle θ_i are computed respectively as

$$R_i=|\mathbf{r}_i-\mathbf{r}_0|=\sqrt{\left(x_i^{'}-x_0^{'}\right)^2+\left(y_i^{'}-y_0^{'}\right)^2+\left(z_i^{'}-z_0^{'}\right)^2}, \tag{11}$$

and $$\theta_i=a\cos\left(\frac{(\mathbf{r}_i-\mathbf{r}_0)\cdot\hat{\mathbf{M}}}{R_i}\right) \tag{12}$$

Since $\hat{\mathbf{M}}$, $x_0^{'}$, and $y_0^{'}$ have been derived in subsection 2.2, unknown parameters in $\tilde{B}_{ir}$ and $\tilde{B}_{iz}$ are $a, z_0^{'}$, and I, while I does not appear in the unit field vector $\tilde{\mathbf{b}}_i$:

$$\tilde{\mathbf{b}}_i=\frac{\tilde{B}_{ir}}{B_i}\hat{\mathbf{r}}+\frac{\tilde{B}_{iz}}{B_i}\hat{\mathbf{M}} \quad , \quad B_i=\sqrt{\tilde{B}_{ir}^2+\tilde{B}_{iz}^2} \tag{13}$$

, where the unit radial vector is $\hat{\mathbf{r}}=\hat{\mathbf{x}}_{loop}\cos\varphi_i+\hat{\mathbf{y}}_{loop}\sin\varphi_i$, and the azimuthal angle is

$$\varphi_i = a\cos\left(\frac{\left(x_i^{'} - r_{0x}^{'}\right)}{\sqrt{\left(x_i^{'} - r_{0x}^{'}\right)^2 + \left(y_i^{'} - r_{0y}^{'}\right)^2}}\right) \quad \text{when} \quad y_i^{'} - r_{0y}^{'} > 0 \quad , \quad \text{and}$$

$$\varphi_i = 2\pi - a\cos\left(\frac{\left(x_i^{'} - r_{0x}^{'}\right)}{\sqrt{\left(x_i^{'} - r_{0x}^{'}\right)^2 + \left(y_i^{'} - r_{0y}^{'}\right)^2}}\right) \text{ when } y_i^{'} - r_{0y}^{'} < 0.$$

On the other hands, the actually recorded unit field vector is $\mathbf{b}_i = \frac{\mathbf{B}_i}{\left|\mathbf{B}_i\right|}$, thus the optimum loop radius, *a*, and the shift of loop center along axis, $z_0^{'}$, should make $\mathbf{b}_i$ parallel to $\tilde{\mathbf{b}}_i$ for the best fit solution.

As a result, the angel between $\mathbf{b}_i$ and $\tilde{\mathbf{b}}_i$, defined as γ_i, is a function of *a* and $z_0^{'}$, that is,

$$\gamma_i = a\cos\left(\mathbf{b}_i \cdot \tilde{\mathbf{b}}_i\right) \tag{14}$$

Thus, one can construct a residue function as

$$\varepsilon\left(a, z_0^{'}\right) = \frac{1}{N}\sum_i \gamma_i \tag{15}$$

Obviously, ε is a function of *a* and $z_0^{'}$. The optimum *a* and $z_0^{'}$ should make ε reach the global minimum in the parameter space. Thus, one can search the global minimum of ε quickly in the 2-D map constituted by *a* and $z_0^{'}$ to find the correspondingly optimum values of *a* and $z_0^{'}$.

Note that, with the knowledge of derived $\hat{\mathbf{M}}$, the inferred location of loop center $\mathbf{r}_0\left(x_0^{'}\hat{\mathbf{x}}_{loop}, y_0^{'}\hat{\mathbf{y}}_{loop}, z_0^{'}\hat{\mathbf{z}}_{loop}\right)$ in the geocentered dipole coordinates can be transformed into the geographic coordinates $\mathbf{r}_0\left(x_0\hat{\mathbf{x}}, y_0\hat{\mathbf{y}}, z_0\hat{\mathbf{z}}\right)$ via Eq. (1).

2.4. The electric current of the loop

Considering the measured field vector $\mathbf{B}_i$, and the field vector induced by the current loop

$$\mathbf{B}_{i0} = \tilde{B}_{ix}\hat{\mathbf{x}}_{loop} + \tilde{B}_{iy}\hat{\mathbf{y}}_{loop} + \tilde{B}_{iz}\hat{\mathbf{M}}, \tag{16}$$

where $\tilde{B}_{ix} = \tilde{B}_{ir} \cos\varphi_i$, $\tilde{B}_{iy} = \tilde{B}_{ir} \sin\varphi_i$, we can construct a dimensionless parameter

$$\delta = \frac{1}{N}\sum_i \frac{|\mathbf{B}_i \text{-} \mathbf{B}_{i0}|}{|\mathbf{B}_i|}, \tag{17}$$

to evaluate the deviation of loop field $\mathbf{B}_{i0}$, from the actual recorded magnetic field $\mathbf{B}_i$.

Since the optimum axis-orientation, the loop center, and the loop radius have been inferred separately in the above subsections, δ becomes the function of only current, I, and the optimum current can be searched when δ reaches the minimum.

The derived loop parameters $\{x'_{0m}, y'_{0m}, z'_{0m}, \theta_{0m}, \varphi_{0m}, a_m, I_m\}$ indeed make δ reach its extremum (see Text S1 in Supplement).

2.5. The summary of technique

Based on the above analysis, the technique steps can be simply summarized as the following:

1. The orientation of the field structure is determined by the loop axis orientation and the loop center. Thus, axis orientation and loop center ($x'_{0m}, y'_{0m}, \theta_{0m}, \varphi_{0m}$) can be searched out firstly by the projection of the measured field vectors.
2. Once the loop axis is determined, the geometry configuration of loop field is only determined by the loop radius and the axis-shift of loop center. Thus, the loop radius (z'_{0m}, a_m) can be resolved by the analysis of field's geometry.
3. Once loop axis, loop center, and the loop radius are solved, the optimum electric current (I_m) can be inverted finally by minimizing the deviation of loop field from the sampled field vectors.

Certainly, to make the inversion more reasonable, one may have to preprocess the data to guarantee that the sampled field data is least contaminated by the external sources, e.g. ionospheric current, before applying the technique.

Test of this technique for, an ideal circular loop field is conducted in Supplement, where the technique successively reproduced the full loop parameters from data along arbitrary trajectory (see Text S2 and Figure S1 to S5 in Supplement). With the same field dataset, the comparison between our technique results and the traditional least-square fitting method demonstrates that our method indeed works better than the least-square fitting (see Text S3 in Supplement).

3. Application to IGRF model

The International Geomagnetic Reference Field (IGRF) is a series of mathematical models describing the large-scale internal part of the Earth's magnetic field between epochs 1900 A.D. and the present (Zmuda 1971). Here, to show the technique applicability and the specific inversion procedures, as an example, we apply the technique to the IGRF model of 12th generation [Thébault et al., 2015]. We could make the comparison of the yielded loop parameters with the well-known eccentric dipole parameters as inferred from the internal Gauss coefficients of IGRF model.

To make the sampled data evenly from IGRF, we construct four synthetic polar circular orbits with same controllable altitude. As shown in Figure 3a, the four polar orbits cross the same pole and cover the longitude 0°-180°, 45°-225°, 90°-270°, and 135°-315°, respectively in the geocentric coordinates. Along each orbit, the spacecraft samples 20 data points evenly of geomagnetic field from IGRF model. In total, 80 data points are obtained from the four orbits. Note that, we use all the Gauss coefficients of IGRF model to compute the sampled field vectors. The IGRF model at the time 2015-01-01 00:00:00 is arbitrarily adopted.

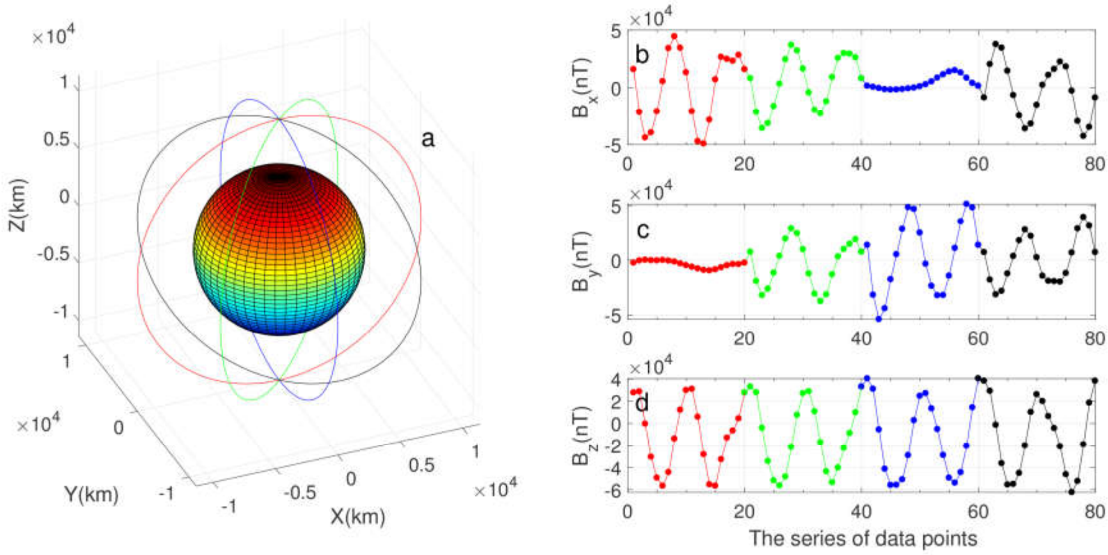

Figure 3. The panel in left column shows the four circular polar orbits with controallable altitude in geocentric coordinates(panel a). In the right column(panel b-d), panels from top to bottom show the series of sampled Bx, By and Bz component, respectively from IGRF model at the time 2015-01-01 00:00:00 when altitudes of the four orbits are zero. The different colored data points correspond to the different colored orbits shown in panel a.

3.1. The case when orbit altitude is zero

We may first consider the case when altitude is zero. In this case, the obtained geomagnetic field data from IGRF could be seen as being sampled on the Earth's surface. Figure 3b shows the series of the sampled 80 magnetic vectors of the four circular orbits in the geocentric coordinates.

With the sampled magnetic field, we calculate α_{min} for all possible orientations of $\hat{\mathbf{M}}(\theta_0, \varphi_0)$ using Eqs. (2-7). In Figure 4a, the 2-D distribution of α_{min} is shown in the map constituted by θ_0 and φ_0.

Obviously, as expected, there are two local minima of α_{min} present in Figure 4a, because the two minima should correspond to the parallel and anti-parallel direction of $\hat{\mathbf{M}}$. After reading the initial values of θ_0 and φ_0 around the two minima, the two candidate directions of $\hat{\mathbf{M}}$, $\hat{\mathbf{M}}_1$ and $\hat{\mathbf{M}}_2$, as well as the corresponding loop centers ($x_0^{'}$, $y_0^{'}$) are derived. The yielded $\hat{\mathbf{M}}_1$ is (θ_0=12.2°, φ_0=297.5°), and $\hat{\mathbf{M}}_2$ is (θ_0=167.7°, φ_0=113.1°), and both of them are nearly anti-parallel to each other.

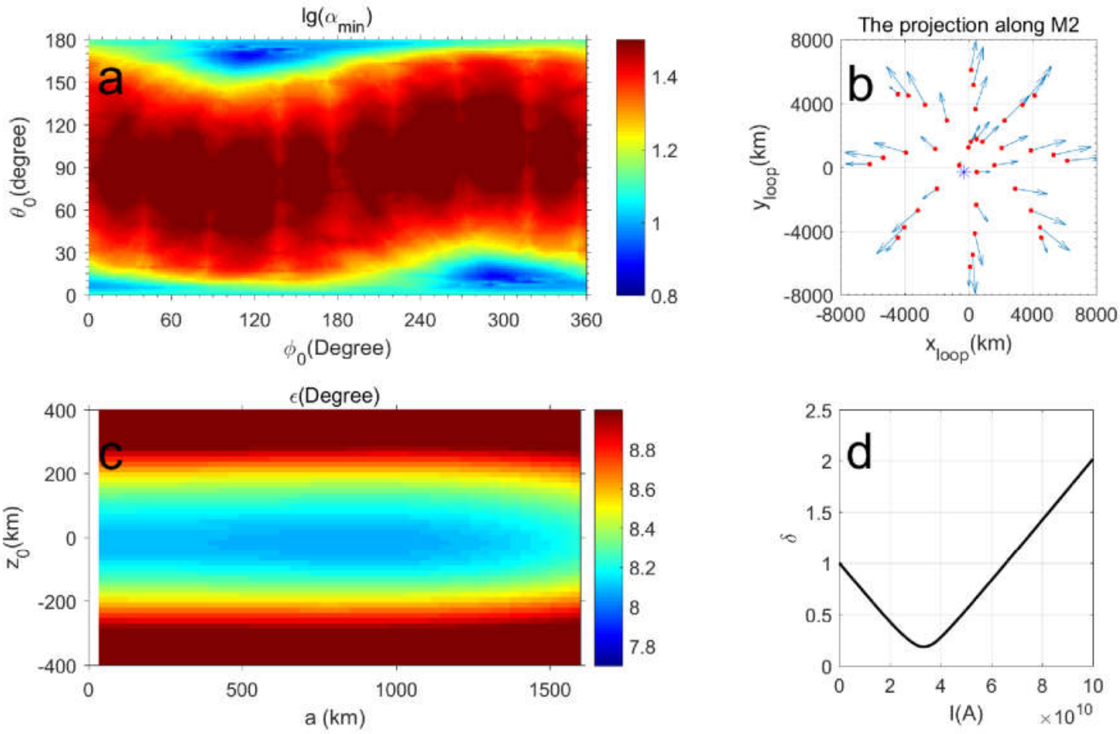

Figure 4. Panel a: The distribution of α_{min} (unit is degree). The logarithm of α_{min} is plot in this panel. Panel b: The projection of magnetic field direction on the equatorial plane of loop coordinates. The red dots represent the location of the spacecraft with $z_i^{'}$> 0, the blue star represents the loop center. Panel c: The 2-D distribution of ε. Panel d: The variation of δ against I.

To determine which one is the final direction of $\hat{\mathbf{M}}$, in Figure 4b, we show the projection of magnetic field vectors on the equatorial plane, i.e. $\mathbf{b}_{ip}$, according to the two candidate axis directions. The projections are only shown when the spacecraft is at the hemisphere in which $\hat{\mathbf{M}}$ is pointing away ($z_i^{'}$> 0, or $\mathbf{r}_i \cdot \hat{\mathbf{M}}$>0). It is clear that, in this hemisphere, the magnetic field vectors basically point radially outward along $\hat{\mathbf{M}}_2$, but inward along $\hat{\mathbf{M}}_1$ (not shown here). Thus, we choose $\hat{\mathbf{M}}_2$ as the final $\hat{\mathbf{M}}$, that is $\hat{\mathbf{M}}$(θ_0=167.7°, φ_0=113.1°). Accordingly, the components of loop center via Eq. (7) are calculated as $x_0^{'}$= -288.6 km and $y_0^{'}$=-325.2 km.

With the derived $\hat{\mathbf{M}}$, $x_0^{'}$ and $y_0^{'}$, Figure 7 shows the distribution of ε via Eq.(15) as a function of a and $z_0^{'}$. With the initial value of $z_0^{'}$ and a read from Figure 4c ($z_0^{'}$=0km, a=800km) , the optimum value of $z_0^{'}$ and a, corresponding to the global minimum of ε, is found to be $z_0^{'}$= -24.5 km, and a= 856 km, respectively.

Finally, with the derived $\hat{\mathbf{M}}$, $x_0^{'}, y_0^{'}, z_0^{'}$ and a, we calculate δ via Eq. (17) with varied current I, and plot the variation of δ against I in Figure 4d. The numerical calculation demonstrates that δ reaches its minimum when I=3.32×10^{10}A.

As a result, the estimated strength of magnetic moment is $M=I\pi a^2$=7.65×10^{22}Am^2, which is comparable to the dipole moment of IGRF (7.72×10^{22}Am^2). The minor discrepancy could owe to the impact of geomagnetic field anomaly on the sampled IGRF field at Earth's surface.

Using Eq. (1), the transformation of the loop center $\mathbf{r}_0$ ($x_0^{'}$= -288.6, $y_0^{'}$= -325.2, $z_0^{'}$= -24.5) km in the loop coordinates into the Cartesian geographic coordinates yields $\mathbf{r}_0$ (x_0= -285.5, y_0=309.3, z_0=111.5) km.

Using the derived loop parameters, the loop field is calculated and shown in Figure 5. Clearly, the inverted loop field shows well-consistence with the sampled IGRF field, which implies that the inverted parameters are reasonable.

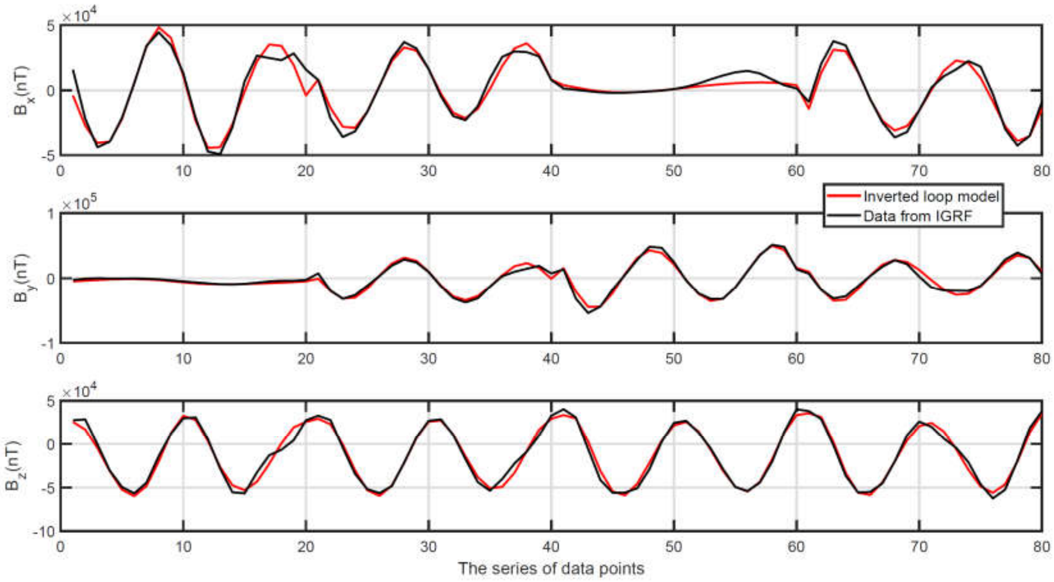

Figure 5. The comparision showing the sampled geomagnetic field from IGRF(black lines) and the magnetic field inverted from the circular loop (red lines).

The derived full loop parameters, the strength of magnetic moment, and the inversion errors are tabulated in Table 1 respectively.

3.2. The cases when orbit altitude is variable

Considering the variable altitude, we repeat the same procedures to check how the inversion results varied with orbit altitude. The calculated results for the other altitudes are also tabulated in Table 1.

We find that, as the orbit altitude increases, the derived parameters are approaching the values of eccentric dipole model with decreasing inversion errors. The results are reasonable, because the field strength of the geomagnetic anomalies or non-dipole components attenuates with altitude more quickly than that of dipole field, and the field at the higher altitude is closer to the dipole field.

Nonetheless, at the very high altitude, as the case of the altitude of 50000km, the sampled field is nearly identical to the dipole field with negligible loop radius. In this case, the numerical inversion would probably fail. The solution of the negligible radius cannot be achieved in the 2-D distribution of ε, unless the tolerance error of numerical calculation is improved.

Table 1. The inverted loop parameters for the IGRF model of the year 2015

Altitude (km)	x_0 (km)	y_0 (km)	z_0 (km)	a (km)	I (*10^{10}A)	M [a] (*10^{22}Am^2)	θ_0 (°)	φ_0 (°)	α_{min} (°)	ε (°)	δ
0	-286	309	111	856	3.32	7.65	167.7	113.1	7.465	8.069	0.185
100	-274	320	95	817	3.66	7.67	167.8	118.0	7.261	7.917	0.179
500	-293	334	71	745	4.41	7.69	168.6	117.4	6.558	6.901	0.156
1000	-310	339	83	701	4.98	7.69	169.1	115.6	5.856	5.997	0.135
2000	-334	348	105	754	4.31	7.71	169.7	113.3	4.843	4.740	0.106
5000	-364	356	170	720	4.73	7.71	171.1	111.8	3.334	2.993	0.064
10000	-381	356	206	631	6.16	7.71	170.9	109.4	2.145	1.848	0.038
20000	-390	357	212	353	19.72	7.71	170.5	108.0	1.276	1.035	0.020
50000 [b]	~	~	~	~	~	~	170.4	107.5	0.581	~	~
ED[c]	-400	352	221	~	~	7.72	170.4	107.4	~	~	~

[a] The magnetic moment M is calculated as $M=\pi I a^2$.
[b] The inversion is failed, because the global minimum of ε cannot be found. Only the derived axis-orientation is tabulated here.
[c] The eccentric dipole (ED) model is adopted, whose displacement of dipole center is calculated only considering the first eight internal Gauss coefficients (See Eqs.(16-18) in Fraser-Smith (1987)). Note, the direction of $\hat{\mathbf{M}}$ is the same in both centered and eccentric dipole models.

4. The application to geomagnetic field data of observatories

Our method does not include the external field sources, such as the ionospheric and magnetospheric currents (tens of nT), and the field induced by the internal induction current due to transient temporal variation of external currents (amplitude is about half of external field) [e.g. Chapman, 1919; Benkova, 1940]. These sources could be seen as the data "noise" as recorded by geomagnetic observatories. Thus, we can apply the technique to the original field data of geomagnetic observatories to check the technique validity in the presence of “noise”.

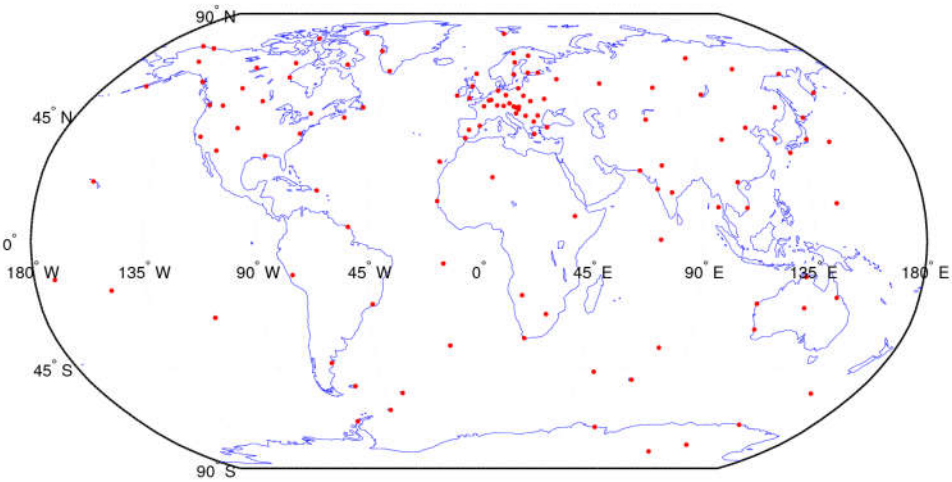

Figure 6. The distribution map of the used geomagnetic observatories.

The used geomagnetic field dataset is from International Real-time Magnetic Observatory Network (INTERMAGNET) which can provide the geomagnetic field data of the global observatories. To facilitate the comparison with the inversion of IGRF field in Section 3, we set the time to sample the geomagnetic field data is at 2015-01-01 00:00:00. The sampled dataset contains 123 data points from 123 observatories (we sample one field vector at each observatory; see Table S2 in Supplement). The distribution map of these observatories is shown in Figure 6.

We tabulate the inverted parameters in Table 2 after performing the technique. The comparison with the test of IGRF’s field on Earth’s surface (see the fourth row of Table 2) shows that the inverted parameters from geomagnetic field data are basically the same with that from the test of IGRF model, which demonstrates that our technique is insensitive to the “noise” component of external currents. The results are reasonable, because the nominal “noise” amplitude due to the space current disturbance is very minor, only about 10^{-3} of the background geomagnetic field strength.

Meanwhile, to check how much the inverted parameters being affected by the regional distribution of observatories, as an example, we perform the technique only considering the observatories in northern hemisphere. The inversion results demonstrate that the loop parameters, especially the radius and current, are significantly different from the parameters calculated from the global observatories though the fitting errors are minor (see Table 2). The inversion results are understandable, because the regional magnetic anomalies could become comparable to the main dipole field, and the sampled data could be biased by these anomalies.

Therefore, to better apply the technique to geomagnetic field data, the sampled geomagnetic observatories should distribute more evenly.

Table 2. The inverted single loop parameters based on the sampled dataset by geomagnetic observatories at the moment of 2015-01-01 00:00:00. The format is the same as Table 1.

Model case	x_0 (km)	y_0 (km)	z_0 (km)	a (km)	I (*10^{10}A)	M (*10^{22}Am^2)	θ_0 (°)	φ_0 (°)	α_{min} (°)	ε (°)	δ
Global [a]	-213	403	128	892	3.08	7.71	172.3	109.2	5.313	8.414	0.175
Northern Hemisphere [b]	-105	127	348	1632	0.87	7.25	176.5	123.8	4.323	8.089	0.149
IGRF data[c]	-286	309	111	856	3.32	7.65	167.7	113.1	7.465	8.069	0.185

[a] The inversion from the dataset of global 123 magnetic observatories
[b] The inversion from the dataset of 95 magnetic observatories in Northern Hemisphere
[c] Same with the first row of Table 1.

5. Comparison with previous' studies

Zidarov and Petrova [1974] fitted the geomagnetic data of 61 magnetic observatories during the period 1932-1960 with one loop model (see Table IV of Zidarov [1985]). Peddie [1979] used 1236 magnetic field component values, or 412 magnetic field vectors near the surface of Earth at the year of 1975 to fit the current loop models. Each field vector was computed from each local spherical harmonic model. Because no specific information of the used dataset was provided by Zidarov and Petrova [1974], and by Peddie [1979], it is difficult to get the same dataset and make direct comparison with their results.

Table 3. The inverted loop parameters for the IGRF model of the year 1960

Method	x_0 (km)	y_0 (km)	z_0 (km)	a (km)	I ($*10^{10}$A)	M ($*10^{22}$Am^2)	θ_0 (°)	φ_0 (°)	α (°)	ε (°)	δ
Our technique	-309	192	86	824	3.69	7.88	167.6	109.4	7.928	7.179	0.170
ZP [a]	-263	263	108	1391	1.33	8.51	169.2	106.8	8.248	7.054	0.169
ED [b]	-366	213	122	~	~	8.03	168.6	110.5	~		~

[a] The loop parameters are adopted from Zidarov and Petrova (ZP) [1974]. Using these loop parameters, the errors α, ε, and δ indicating the deviation of the loop field from the sampled IGRF field are calculated by Eq. (3), Eq.(15), and Eq. (17), respectively.

[b] The eccentric dipole (ED) center is adopted from Fraser-Smith using Gauss coefficients[1987].

Table 4. The inverted loop parameters for the IGRF model of the year 1975. The format is the same with Table 3.

Method	x_0 (km)	y_0 (km)	z_0 (km)	a (km)	I ($*10^{10}$A)	M ($*10^{22}$Am^2)	θ_0 (°)	φ_0 (°)	α (°)	ε (°)	δ
Our technique	-300	210	108	643	6.01	7.81	167.7	110.8	8.020	7.321	0.174
Peddie [a]	-318	259	124	1021	2.43	7.95	169.2	108.7	8.25	7.229	0.171
ED[b]	-379	237	160	~	~	7.94	168.8	109.5	~		~

[a] The parameters are adopted from the unstrained single loop model of Peddie [1979].

[b] It is adopted from Fraser-Smith[1987] using Gauss coefficients.

Here, to show a simple comparison with Zidarov and Petrova [1974], and with

Peddie [1979], we just invert the loop parameters based on the IGRF field at the moment of 1960-01-01 00:00:00 and 1975-01-01 00:00:00. Our inversion results are tabulated in Table 3 and Table 4, respectively. In our inversion, the altitudes of the four circular orbits in Figure 3 are assumed to be zero, so that the sampled data could be seen as the measured field on Earth's surface.

From Table 3 and Table 4, we can see that our inverted parameters show some differences, especially the loop radius and current, with that derived by Zidarov and Petrova [1974], and by Peddie [1979]. The reasons for the difference, in addition to the inversion methods, we believe it could be induced also by the different field datasets since the bias of magnetic observatories distribution could significantly affect the inversion (see Section 4).

It is worthy to note that, by applying to the same sampled IGRF field dataset, although the parameters by Zidarov and Petrova [1974], and by Peddie [1979] yield comparable error δ with ours, their derived $\hat{\mathbf{M}}$ shows larger error σ. In other words, the different sets of loop parameters may yield comparable δ for a same field dataset. Thus, it is insufficient to evaluate the fitting by minimizing error for only one criterion [e.g. Zidarov and Petrova, 1974; Zidarov, 1985; Peddie, 1979], but need comprehensively several criteria such as for axis orientation, field geometry, and the relative deviation of field strength.

6. Prospect of further applications

In the further technique applications, several tips below are worthy to be noticed:

1) The technique we presented based on Eqs. (2-7) to find the axis orientation could be also applied to the other internal magnetic sources whose current systems are azimuthally symmetric, e.g. the disk-like currents, the spherical shell-like, and the ball-like currents etc., because the field generated by such current systems has no azimuthal component in principle.

2) Our loop model can be reduced easily to the dipole model by reducing the loop radius a to zero. In this case, only six parameters are needed to be inverted (two parameters for the axis orientation, three parameters for the dipole center, and one parameter for the amplitude of dipole moment). Eqs. (2-7) to find the axis orientation still holds on for the dipole model, while the angle γ defined in Eq. (14) becomes function of only $z_0^{'}$. After solving axis orientation and dipole center, the dipole moment strength can be determined similarly by Eq. (17). The dipole model could be considered when the optimum loop radius cannot be searched.

3) The algorithm can be extrapolated to the model of currents on a spherical surface, which could be closer to the real dynamo current systems than the loop model. It also needs seven parameters to characterize the spherical surface model (two parameters for the axis orientation, three parameters for the spherical center, one parameter for the spherical radius, and one parameter for the surface current density if it is only vaired with latitude). The technique application to the spherical surface model will be studied in next step.

4) The single loop could be extrapolated to the multiple loops to include the contributions of crustal fields or local anomaly fields. If we label the measured

magnetic field vector as **B**, the magnetic field vector expected from the single loop is $\mathbf{B}_{L1}$, then we would have the deviation $\mathbf{\Delta}_1=\mathbf{B}-\mathbf{B}_{L1}$. We can repeat the procedures to fit $\mathbf{\Delta}_1$ using the second current loop. If the field from the second loop is labeled as $\mathbf{B}_{L2}$, the resulted field deviation becomes $\mathbf{\Delta}_2=\mathbf{\Delta}_1-\mathbf{B}_{L2}$. We can iterate the algorithm until the deviation becomes acceptable. The technique of multiple loops could be applied also to model the planetary crustal fields or the regional anomaly fields, like the Lunar crustal fields and Martian crustal fields. We will try the model of multiple loops in next studies.

5) Our loop model also benefits the study of secular variation of geomagnetic field. By application to the field dataset of long period, the evolved loop parameters over the long period could probe the secular variation of geomagnetic or planetary field. We could survey the 100 years variation of geomagnetic field by continue the IGRF test in future study.

6) Geomagnetic palaeosecular variation based on current loop model were conducted in previous studies [e.g. Roy and Wagner, 1982], but the initial estimates of parameters are required in the fitting. Thus, it is expected that, with our new technique, the application into the paleomagnetic data is worth re-examining.

7. Discussions

We have to remind that the inverted parameters depend strongly on the sampled field dataset. Therefore, when deep dynamo (the poloroidal field component) is modeled, field components of crustal field in the dataset should be negligible. In this case, our technique could be better applied to the dataset with higher altitude, e.g. the magnetometer data of spacecraft (such as Swarm mission) after subtracting the external field, because the crustal fields would attenuate quickly with altitude.

It is noteworthy that, since the observed field is the integral product of all the current sources, the magnetic inversion usually has multi-solutions. One would probably never be able to seperate the real interior current sources exactly, no matter how perfect and complete the magnetic field models above planetary surface are built [see page 42 of Merrill, McElhinny, & McFadden, 1996]. Therefore, although our technique works well to invert the loop model, it should be emphasized and cautioned that the current loop model we addressed here cannot be the absolute pattern of interior currents, and the obtained loop parameters could be only seen as the equivalent parameters of the whole internal current patterns.

Considering the nonuniqueness of inversion solution, we have to interpret the physical meanings of the yielded loop parameters carefully. Our inversion results show that the loop center is eccentric, and displaced towards Eastern Hemipshere. The yielded displacement of loop center could not be a trivial output. The dynamo simulations showed that the displacement could be caused by the lopsided inner core growth [Olson and Deguen, 2012], and the displacement of loop center may indicate that Earth's inner core is solidifying in the western hemisphere and melting in the east [Bergman, 2010].

Both tests of IGRF field and geomagnetic field of observatories show that the inferred equivalent loop radius is about 700-900 km (see Tables 1-3). This result appears unreasonable, because it may indicate that the geodynamo currents can extend deeper into the inner solid core (the radius of solid core is about 1265km). Our test shows that the inversion with source of current flowing on a spherical surface would result in loop radius smaller than the spherical radius, and the successful run of inversion implies that the surface current should concentrate more in magnetic equator than that regulated by $\sin\theta$ (θ is magnetic colatitude) (see Text S4, Figure S6 and Table S1 in Supplement). Thus, if the real dynamo currents can be well-seen flowing on spherical surface (e.g. the surface of inner core), the loop with radius smaller than the inner core radius could make sense. Meanwhile, the successful inversion of loop radius may indicate that the surface current would concentrate more near the spherical equator than that regulated by $\sin\theta$.

To develop the inversion technique of more plausible spherical surface model should be considered in next study.

8. Conclusions

In this paper, we developed a new technique to invert the geomagnetic field based on a single circular current loop model. The inverted loop parameters are meaningful to interpret the geometric characteristics of deep dynamo currents. This technique is able to effectively separate and solve the loop parameters successively, that is, the full optimum parameters can be quickly searched, showing advantage over the previous least-square fitting method. Model is examined against geomagnetic field (both IGRF models and the measured geomagnetic field of observatories) to demonstrate the reasonability and feasibility of this technique. To reduce the influence of the local magnetic anomaly, the technique is suggested to be applied at higher altitude. Not only is the loop algorithm flexible to be reduced to a dipole model, but also it is able to be extrapolated to a spherical surface model.

Declarations

List of abbreviations

SHA: Apherical Harmonic Analysis

IGRF: International Geomagnetic Reference Field

ED: Eccentric Dipole

INTERMAGNET: International Real-time Magnetic Observatory Network

Availability of data and materials

The IGRF model used in this paper is available at the website https://www.ngdc.noaa.gov/IAGA/vmod/igrf.html. The global geomagnetic field data in INTERMAGNET can be accessed at http://www.intermagnet.org/index-eng.php. The Matlab code used in this study are available on request.

Competing interests

The authors declare that they have no competing interests.

Funding

This work is supported by the Strategic Priority Research Program of Chinese Academy of Sciences (Grant No. XDA17010201), by the Key Research Program of the Institute of Geology & Geophysics, CAS, Grant No. IGGCAS- 201904, and also by the National Natural Science Foundation of China (grants 41774188, 41922031, 41525016, and 41621063).

Authors' contributions

ZR designed and conducted this study. MY, DK, and JC helped to edit the text. All authors read and approved the final manuscript.

Acknowledgments

The IGRF model used in this paper is available at the website https://www.ngdc.noaa.gov/IAGA/vmod/igrf.html. The authors are thankful to the INTERMAGNET and contributing observatories (Table S2) for providing the global geomagnetic field data, which is available at the website http://www.intermagnet.org/index-eng.php. The authors thank P. W. Livermore, J. A. Slavin, Y. X. Pan, J. H. Zhang, Z. G. Zhang, and K. K. Zhang for the helpful discussions.

Supplementary Information

Additional file 1:

Text S1. The mathematical proof of the extremum of δ.

Text S2. Inversion with magnetic source of single loop.

Text S3. Comparison with the non-linear fitting method.

Text S4. Inversion with magnetic source of current on a spherical surface.

Figure S1. The time series of magnetic field along spacecraft's trajectory.

Figure S2. The distribution of $\alpha_{\min}$. To identify the global minimum easily, we show the distribution of lg($\alpha_{\min}$) in this plot.

Figure S3. The projection of magnetic field direction on the equatorial plane of loop coordinates. The red dots represent the location of spacecraft with $z_i^{'} > 0$, the blue arrows are the projected directions of sampled field vectors, and the red square represents the loop center.

Figure S4. The 2-D distribution of ε.

Figure S5. The variation of δ against I.

Figure S6. Test with four orbits on the magnetic field whose source is the current on a spherical surface. The distribution of surface current density j=0.2*$sin\theta$ is colored.

Table S1. The inversed single loop parameters when magnetic source is the current flowing on a spherical surface.

Table S2. The geomagnetic field data of global geomagnetic observatories recorded on 2015-01-01 00:00:00. The columns from left to the right show the IAGA name of observatories, the latitude and longitude of observatories, the northward (X), the eastward (Y), the downward (Z) component, and the field strength (F) of geomagnetic field in the local geographic coordinates, respectively. The unavailable data is assigned as 99999. The field data can be also accessible at the website http://www.intermagnet.org/index-eng.php

Reference

1. Alldredge, L. R., and L. Hurwitz (1964), Radial dipoles as the sources of the Earth's main magnetic field, J. Geophys. Res., 69(12), 2631–2640, doi:10.1029/JZ069i012p02631.
2. Alldredge, L. R., and C. O. Stearns (1969), Dipole model of the sources of the Earth's magnetic field and secular change, J. Geophys. Res., 74(27), 6583–6593, doi:10.1029/JB074i027p06583.
3. Alldredge, L.R. (1987), Current loops fitted to geomagnetic model spherical harmonic coefficients, *J. Geomag. Geoelec*., 39, 271-296.
4. Amit, H., Olson, P. (2008). Geomagnetic dipole tilt changes induced by core flow. Phys. Earth Planet. Inter., 166, 226-238.
5. Anderson, B. J., et al. (2011). The global magnetic field of Mercury from MESSENGER orbital observations. Science, 333, 1859–1862. https://doi.org/10.1126/science.1211001
6. Benkova, N. P. (1940), Spherical harmonic analysis of the Sq-variations, May-August 1933, Terrest. Magnetism. Atmospheric Elec., 45, 425-432.
7. Benton, E. R. and L. R. Alldredge (1987). On the interpretation of the geomagnetic energy spectrum. Physics of the Earth and Planetary Interiors, 48, 265-278.
8. Bergman, M. (2010). An inner core slip-sliding away. Nature, 466, 697–698.
9. Bochev, A. Z., Presenting the Earth's magnetic field as a field of six optimal dipoles, C. R. Acad. Bulg. Sci., 28(4), 469-471, 1975.

10. Cain, J. C., Schmitz, D. R. & Kluth, C. Eccentric geomagnetic dipole drift. Phys. Earth Planet. Inter. 39, 237–242 (1985).

11. Chapman, S.(1919), The solar and lunar diurnal variation of the earth's magnetism, Phil. Trans. Roy. Soc. London, A, 218, 1-118.

12. Chapman, S., & Bartels, J. (1940). Geomagnetism (pp. 639–668). New York: Oxford University Press.

13. Connerney, J. E. P. (1993), Magnetic fields of the outer planets, *J. Geophys. Res.*, 98(E10), 18659–18679, doi:10.1029/93JE00980.

14. Constable, C. G. and Constable, S. C. (2004) Satellite Magnetic Field Measurements: Applications in Studying the Deep Earth, in The State of the Planet: Frontiers and Challenges in Geophysics (eds R.S.J. Sparks and C.J. Hawkesworth), American Geophysical Union, Washington, D. C.. doi: 10.1029/150GM13

15. Demina, I. M. and Yu. G. Farafonova (2016), Inverse Problem for the Current Loop Model: Possibilities and Restrictions, *Geomagn. Aeron*., 56, 415–425.

16. Fraser‐Smith, A. C. (1987), Centered and eccentric geomagnetic dipoles and their poles, 1600–1985, Rev. Geophys., 25(1), 1–16, doi:10.1029/RG025i001p00001.

17. James, R. W. & Winch, D. E. The eccentric dipole. Pure Appl. Geophys. 66, 77–86, (1967).

18. Johnson, C. L., et al. (2012), MESSENGER observations of Mercury’s magnetic field structure, J. Geophys. Res., 117, E00L14, doi: 10.1029/2012JE004217.

19. Knoepfel, H.E. (Eds.). (2000). Magnetic Fields: A Comprehensive Theoretical Treatise for Practical Use, New York, Wiley.

20. Mayhew, M.A. and Estes, R.H. (1983), Equivalent source modeling of the core magnetic field using Magsat data, J. Geomagn. Geoelectr., 35(4), pp. 119–130.

21. Merrill, R. T., McElhinny, M. W., & McFadden, P. L. (Eds.). (1996).The Magnetic Field of the Earth: Paleomagnetism, the Core, and the Deep Mantle (pp.17-46). Academic Press, San Diego, Calif.

22. McNish, A. G., Physical representations of the geomagnetic field, Eos Trans. AGU, 21, 287-29l, 1940.

23. Olsen, N., K.-H. Glassmeier, and X. Jia (2010), Separation of the magnetic field into external and internal parts, Space Sci. Rev., 152(1–4), 135–157, doi: 10.1007/s11214-009-9563-0.

24. Olson, P., Deguen, R. Eccentricity of the geomagnetic dipole caused by lopsided inner core growth. Nat. Geosci. 5 (8), 565–569, 2012.

25. Peddie, N. W. (1979), Current loop models of the Earth's magnetic field, *J. Geophys. Res.*, 84(B9), 4517–4523, doi:10.1029/JB084iB09p04517.

26. Pudovkin, I. M., and V. I. Kolesova (1968), Dipole model of the main geomagnetic field (based on an analysis of the Z_{ao} field), Geomagn. Aeron. (Engl.transl.), 8(2), 301-302.

27. Roy, M., J. -J. Wagner (1982), Palaeosecular variation and the current loop model of the geomagnetic field, *Geophysical Journal International*, 71(1), 269–273, https://doi.org/10.1111/j.1365-246X.1982.tb04999.x

28. Schubert, G. and K.M. Soderlund (2011), Planetary magnetic fields: Observations and models, Physics of the Earth and Planetary Interiors, 187, 92–108.
29. Thébault, E., et al. (2015), International Geomagnetic Reference Field: The 12th generation, *Earth Planets Space*, **67**(1), doi:10.1186/s40623-015-0228-9.
30. Lyakhov, B. M. (1960), The Earth's magnetic field as a sum of two dipole fields (in Russian), Izv. Akad. Nauk SSSR Set. Geofiz., 4, 601-606.
31. Zmuda, A.J. (1971), The International Geomagnetic Reference Field: introduction, Bull. Int. Assoc. Geomag Aeronomy, 28,148 – 152.
32. Zidarov, D.P., and T. Petrova (1974), Representation of the earth's magnetic field as a field of a circular loop, C. R., Acad. Bulg. Sci., 27, 203-206.
33. Zidarov, D. P. (1985), Earth's magnetic field modelling and Earth's structure and evolution, *Phys. Earth Planet. Int.*, 37, 74–86.

Supporting Information for

New technique to diagnose the geomagnetic field based on the single circular current loop model

Z. J. Rong[1, 2, 3], Y. Wei[1, 2, 3], M. Yamauchi[4], W. Y. Xu[1], D. L. Kong[5], J. Cui[6], C. Shen[7], R. X. Zhu[1, 2], W. X. Wan[1, 2, 3], J. Zhong[1, 2, 3], L. H. Chai[1, 2, 3]

[1]Key Laboratory of Earth and Planetary Physics, Institute of Geology and Geophysics, Chinese Academy of Sciences, Beijing 100029, China

[2]College of Earth and Planetary Sciences, University of Chinese Academy of Sciences, Beijing, China

[3]Beijing National Observatory of Space Environment, Institute of Geology and Geophysics, Chinese Academy of Sciences, Beijing, China

[4]Swedish Institute of Space Physics, Kiruna, Sweden

[5]School of Atmospheric Sciences, Sun Yat-Sen University, Zhuhai 519082, China.

[6]Shanghai Astronomical Observatory, Chinese Academy of Sciences, Shanghai 200030, China

[7]Harbin Institute of Technology, Shenzhen, China,

Contents of this file

Introduction

This supplementary information contains additional details of the technique tests and the geomagnetic field dataset that we present in the paper. We provide the theoretic proof that the inverted parameters from our technique can make δ reach its extremum (Text S1). We apply the technique to the ideal circular loop field, and show that this technique is able to invert the full loop parameters exactly (Text S2, Figure S1 to S5). We compare the inversion results with the traditional least-square fitting method (Text S3). We test the technique when the magnetic source is current flowing on a spherical surface (Text S4, Table S1). Table S2 lists the geomagnetic field dataset used in Section 4.

Text S1.

<u>The mathematical proof of the extremum of δ</u>

The dimensionless error δ defined in Eq. (17) of body text is, in principle, the function of the full loop parameters {$x_0^{'}, y_0^{'}, z_0^{'}$, θ_0, φ_0, a, I}. Here, we show that, the derived loop parameters {$x_{0m}^{'}$, $y_{0m}^{'}$, $z_{0m}^{'}$, θ_{0m}, φ_{0m}, a_m, I_m} from our technique indeed make δ reach its extremum.

Because α in Eq.(3) is the function of {$x_0^{'}, y_0^{'}$, θ_0, φ_0}, $\alpha_{\min}$ is the function of {θ_0, φ_0}, and ε in Eq.(15) is the function of {$z_0^{'}$, a}, δ is actually the function of {σ, ε, I}. The extremum of δ is reached when all the partial differential solutions of δ equal zero. Obviously, when $x_0^{'} = x_{0m}^{'}$, $y_0^{'} = y_{0m}^{'}$, we have $\frac{\partial\delta}{\partial x_0^{'}} = \frac{\partial\delta}{\partial\alpha}\frac{\partial\alpha}{\partial x_0^{'}} = 0$ and $\frac{\partial\delta}{\partial y_0^{'}} = \frac{\partial\delta}{\partial\alpha}\frac{\partial\alpha}{\partial y_0^{'}} = 0$. Similarly, when $x_0^{'} = x_{0m}^{'}$, $y_0^{'} = y_{0m}^{'}$, $\theta_0 = \theta_{0m}$, $\varphi_0 = \varphi_{0m}$, we have $\frac{\partial\delta}{\partial\theta_0} = \frac{\partial\delta}{\partial\alpha}\frac{\partial\alpha}{\partial\alpha_{\min}}\frac{\partial\alpha_{\min}}{\partial\theta_0} = 0$, and $\frac{\partial\delta}{\partial\varphi_0} = \frac{\partial\delta}{\partial\alpha}\frac{\partial\alpha}{\partial\alpha_{\min}}\frac{\partial\alpha_{\min}}{\partial\varphi_0} = 0$ .In the same way, when $x_0^{'} = x_{0m}^{'}$, $y_0^{'} = y_{0m}^{'}$, $\theta_0 = \theta_{0m}, \varphi_0 = \varphi_{0m}$, $z_0^{'} = z_{0m}^{'}$, $a = a_m$, we have $\frac{\partial\delta}{\partial z_0^{'}} = \frac{\partial\delta}{\partial\varepsilon}\frac{\partial\varepsilon}{\partial z_0^{'}} = 0$ and $\frac{\partial\delta}{\partial a} = \frac{\partial\delta}{\partial\varepsilon}\frac{\partial\varepsilon}{\partial a} = 0$. Finally, when $x_0^{'} = x_{0m}^{'}$, $y_0^{'} = y_{0m}^{'}$, $\theta_0 = \theta_{0m}, \varphi_0 = \varphi_{0m}$, $z_0^{'} = z_{0m}^{'}$, $a = a_m$, $I = I_m$, we have $\frac{\partial\delta}{\partial I} = 0$.

In other words, the loop parameters {$x_{0m}^{'}, y_{0m}^{'}, z_{0m}^{'}$, θ_{0m}, φ_{0m}, a_m, I_m} from our technique can make all the partial differential solutions of δ equal zero, and δ must reach its extremum with the derived loop parameters.

Text S2.

<u>Inversion with magnetic source of single loop</u>

To test the validity of this technique, we construct a circular current loop model with given parameters to generate the loop field which is sampled by a virtual spacecraft along an arbitrary trajectory. If the algorithm of technique is valid, the application to the sampled dataset should be able to invert the loop parameters exactly.

The input loop parameters are like this: the location of loop center is at $\mathbf{r}_0$ (x_0=0.1, y_0=0.2, z_0=0.5) m, the loop radius is a=0.5m, the carried electric current is I=0.35A, and the loop axis orientation is $\hat{\mathbf{M}}$ (θ_0=60°, φ_0=40°).

Using these loop parameters, the sampled magnetic field data can be analytically computed via Eqs. (8-12). The test here is to apply our technique with the sampled magnetic field to invert the input parameters $\mathbf{r}_0$, a, I, and $\hat{\mathbf{M}}$.

The spacecraft's trajectory is arbitrarily assumed to be linearly varied from (x= -2, y= -2, z= -2) m to (x=2, y=2, z=2) m, and spacecraft evenly records the magnetic field with, arbitrarily, 20 data points. The time series of the sampled magnetic field are shown in Figure S1.

Using Eqs. (2)-(7), we calculate $\alpha_{\min}$ for all possible orientations of $\hat{\mathbf{M}}$ (θ_0, φ_0). In Figure S2, we show the 2-D distribution of $\alpha_{\min}$ in the map constituted by θ_0 and φ_0. Obviously, as expected, there are two global minima of $\alpha_{\min}$ present in Figure S2. One is about at (θ_0=60°, φ_0=45°), the other one is about at (θ_0=120°, φ_0=225°). The two minima should correspond to the parallel and anti-parallel direction of $\hat{\mathbf{M}}$. With the reading of the initial values of θ_0 and φ_0 around the two minima, the two optimum candidate directions of $\hat{\mathbf{M}}$, $\hat{\mathbf{M}}_1$ and $\hat{\mathbf{M}}_2$, as well as the corresponding loop centers ($x_0^{'}$, $y_0^{'}$) are derived. The yielded $\hat{\mathbf{M}}_1$ is (θ_0=60°, φ_0=40°), and $\hat{\mathbf{M}}_2$ is (θ_0=120°, φ_0=220°), and both of them are nearly anti-parallel to each other.

To determine which one is the final direction of $\hat{\mathbf{M}}$, in Figure S3, we show the projection of magnetic field vectors on the equatorial plane, i.e. $\mathbf{b}_{ip}$, according to the two candidate axis directions. In Figure S3, the projections are only shown when spacecraft is at the hemisphere $\hat{\mathbf{M}}$ pointing away ($z_i^{'} > 0$, or $\mathbf{r}_i \cdot \hat{\mathbf{M}} > 0$). It is clear that, in this hemisphere, the magnetic field vectors basically point radially outward along $\hat{\mathbf{M}}_1$ (see Figure S3a, one inward magnetic vector is actually induced by the axis shift of the loop center), but inward along $\hat{\mathbf{M}}_2$ (see Figure S3b). Thus, we choose $\hat{\mathbf{M}}_1$ as the final optimum direction of $\hat{\mathbf{M}}$, that is $\hat{\mathbf{M}}$(θ_0=60°, φ_0=40°). Accordingly, the components of loop center via Eq. (7) are calculated as $x_0^{'}$= -0.2455 m and $y_0^{'}$= -0.2383 m.

Further, as shown in Figure S4, with the derived $\hat{\mathbf{M}}$, $x_0^{'}$ and $y_0^{'}$, the distribution of ε can be plotted as a function of $z_0^{'}$ and a via Eq.(15). Consequently, with the initial optimum value of $z_0^{'}$ and a from Figure S4 ($z_0^{'}$= a =0.5 m) , the optimum value of $z_0^{'}$ and a, corresponding to the global minimum of ε, is found to be $z_0^{'}$=0.4277 m, and a=0.5 m, respectively.

Finally, with the derived $\hat{\mathbf{M}}$, $x_0^{'}, y_0^{'}, z_0^{'}$ and a, we calculate δ via Eq. (17) with varied current I, and plot the variation of δ against I in Figure S5. The numerical calculation demonstrates that δ reaches its minimum when I=0.35 A via Eq. (17).

Using Eq. (1), the transformation of the loop center $\mathbf{r}_0$ ($x_0^{'}$=-0.2455, $y_0^{'}$=-0.2383, $z_0^{'}$ =0.4277) m in the loop coordinates into the Cartesian coordinates yields $\mathbf{r}_0$ = (x_0=0.1, y_0=0.2, z_0=0.5) m. Considering the inverted $\hat{\mathbf{M}}$(θ_0=60°, φ_0=40°), a=0.5 m, and I=0.35 A, obviously, our technique can exactly invert the full parameters of a circular current loop model if the sampled magnetic field is the ideal loop field.

Text S3.

<u>Comparison with the non-linear fitting method</u>

In the "Introduction" of text body, we state that all the past methods employed the least-square fitting methods to fit the loop parameters simultaneously. Here, with the same sampled field dataset in **Text S2**, we show the comparison of our technique with the fitting method.

The three Cartesian components of the sampled magnetic field vectors are denoted as B_{ix}, B_{iy}, and B_{iz}. While, the field components predicted by the loop model are B_{iX}, B_{iY}, and B_{iZ}, which are the functions of the loop parameters $\mathbf{r}_0$, a, I, and $\hat{\mathbf{M}}$. B_{iX}, B_{iY}, and B_{iZ} can be calculated via Eqs.(8-12). We can construct a least-square residual error as

$$Res\left(\mathbf{r}_0, a, I, \mathbf{M}\right) = \sum_i \left[\frac{\left(B_{ix} - B_{iX}\right)^2 + \left(B_{iy} - B_{iY}\right)^2 + \left(B_{iz} - B_{iZ}\right)^2}{B_{ix}^2 + B_{iy}^2 + B_{iz}^2} \right]^{1/2}$$

The optimum parameters should make the residual error, *Res*, reach the minimum, which could be solved by the function demand "**fminsearch**" of **Matlab.**

As expected, the yielded fitting parameters is indeed strongly dependent on the initial input parameters we chosen. If the initial parameter set is not far from the real parameters, for example, chosen as {$\mathbf{r}_0$ (x_0=0.08, y_0=0.1, z_0=0.4) m; a=0.4m; I=0.3A; **M**= (θ_0=65°, φ_0=45°)}, then the real parameters can be well fitted by the optimization, that is{$\mathbf{r}_0$ = (x_0=0.1, y_0=0.2, z_0=0.5) m; a=0.5m; I=0.35A; **M** (θ_0=60°, φ_0=40°)}.

In contrast, if the initial parameters are set as {$\mathbf{r}_0$ (x_0=0, y_0=0, z_0=0) m; a=0.5m; I=0.35A; **M** (θ_0=60°, φ_0=40°)}, then the output shows that optimization calculation quits due to exceeding the iteration times, and the returned parameters yields {$\mathbf{r}_0$ (x_0=0.14, y_0=0.40, z_0=0.08) m; a=0.61m; I=0.21A; **M** (θ_0=61.99°, φ_0=46.33°)}.

Obviously, in comparison with the least-square fitting, our technique can effectively avoid the dilemma of setting initial values.

Text S4.

Inversion with magnetic source of current on a spherical surface

Although our technique works well for the ideal loop currents, it is still unknown whether it works well for the other more complicated current patterns. To test the technique ability for the complicated currents pattern, the pattern of dynamo current could be more plausible seen as the current flowing on a spherical surface instead of the loop current.

According to the Biot-Savart law, the magnetic field generated by the current flowing on a spherical surface can be calculated as

$$\mathbf{B}(x,y,z)=\frac{\mu_0}{4\pi}\iint\frac{jd\mathbf{s}\times\mathbf{R}}{R^3}$$

Where, j is the surface current density, and **R** is the displacement vector to the spherical center.

Here, to simplify the calculation, we assume that j is only dependent on the polar angle (colatitude), and considered the cases when $j=j_0*cos^2\theta$, $j_0*(cos^2\theta)^{1/2}$, j_0, $j_0*sin\theta$, $j_0*sin^2\theta$, $j_0*sin^5\theta$, $j_0*sin^{10}\theta$, $j_0*sin^{20}\theta$, and $j_0*sin^{50}\theta$, respectively.

As shown in Figure S6, in a given Cartesian coordinate, the input parameters are arbitrarily specified, that is, $\mathbf{r}_0$ =(x_0=0, y_0=0.2, z_0=0.3) m, a=0.5 m, j_0=0.2 Am^{-2}, and $\hat{\mathbf{M}}$ = (θ_0=45°, φ_0=150°).To make the sampled data evenly, four polar circular orbits with radius being 1 m are constructed. The longitude coverage of the four orbits are the same as that studied in Section 3.1. Along each orbit, 20 data points are sampled. In total, 80 field vectors are obtained from the four orbits.

After performing our technique for the different cases of surface current density distributions, the yielded loop parameters are tabulated correspondingly in Table S1.

It is clear from Table S1 that the loop model can well recover the displacement of sphere center and the magnetic axis orientation if the surface currents are flowing purely azimuthally. Interestingly to note that, for the cases of $j= j_0*cos^2\theta$, $j_0*(cos^2\theta)^{1/2}$, j_0 and $j_0*sin\theta$, the optimum loop radius cannot be find, and the inversion calculation is aborted. The failure of inversion in these cases is understandable, because the external field of $j= j_0*sin\theta$ is the ideal dipole field whose loop radius is zero (see http://photonics101.com/magnetostatic-fields-in-matter/surface-current-on-sphere). As j increases with the latitude, e.g. $j= j_0$, $j_0*(cos^2\theta)^{1/2}$, $j_0*cos^2\theta$, the induced external fields are more elongated than the dipole field along magnetic axis orientation, thus the optimum loop radius cannot be inverted also.

In contrast, as j becomes concentrated more than $j_0*sin\theta$ towards magnetic equatorial plane, e.g. $j= j_0*sin^2\theta$, $j_0*sin^5\theta$, $j_0*sin^{10}\theta$, $j_0*sin^{20}\theta$, and $j_0*sin^{50}\theta$, our inversion calculation can be performed successfully. The inversion results demonstrate that: 1. the equivalent loop radius is smaller than the real spherical radius; 2. the loop radius is approaching the real spherical radius as j concentrates more in magnetic equatorial plane.

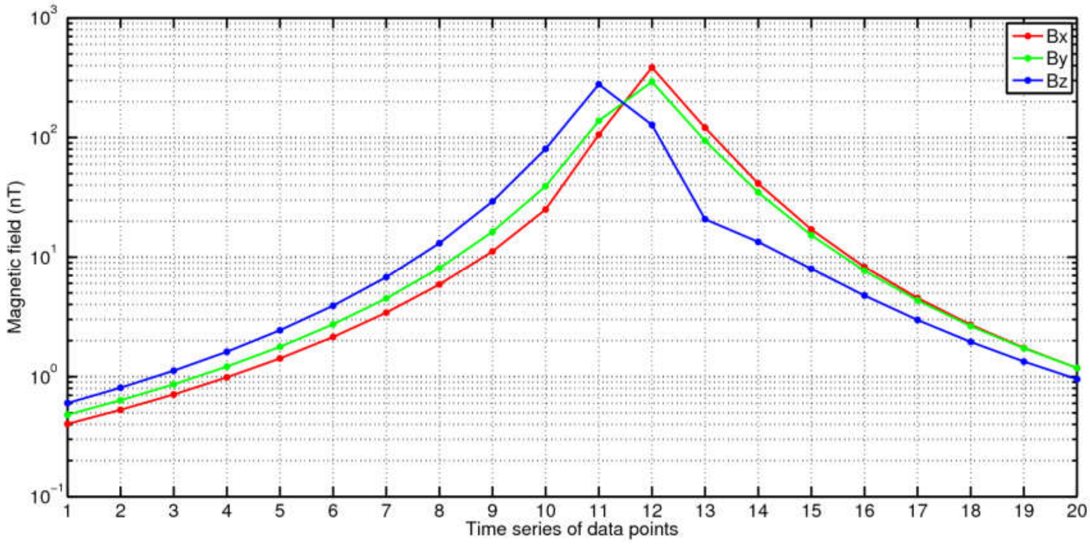

Figure S1. The time series of magnetic field along spacecraft's trajectory.

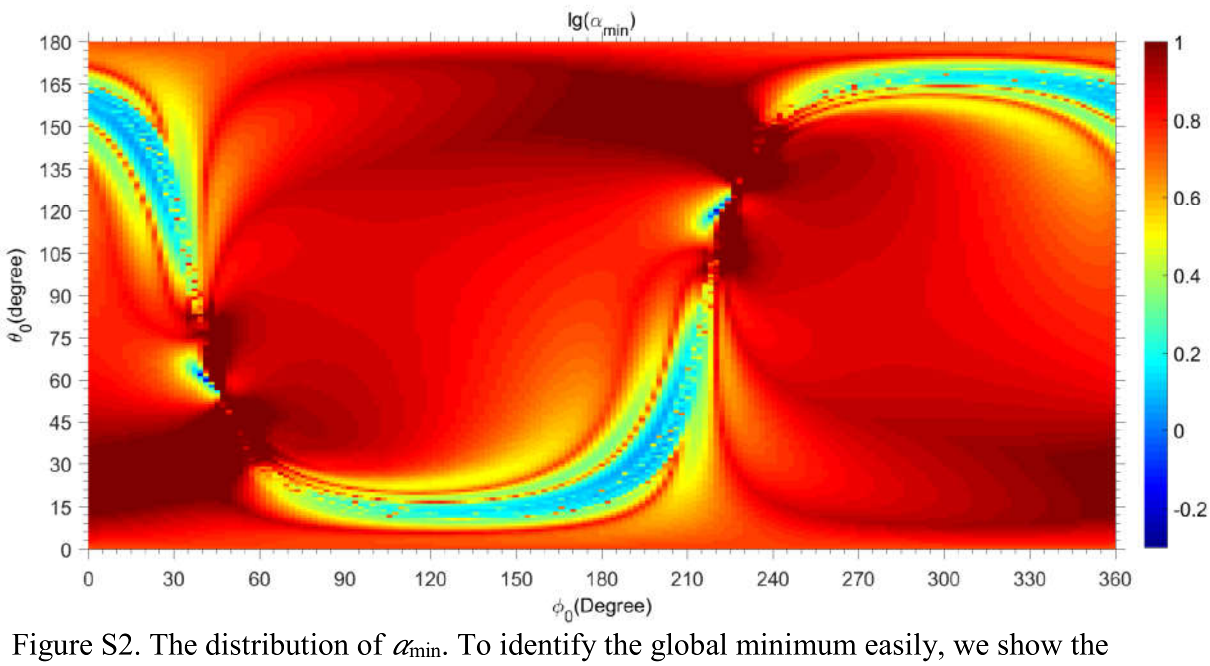

Figure S2. The distribution of $\alpha_{\min}$. To identify the global minimum easily, we show the distribution of lg($\alpha_{\min}$) in this plot.

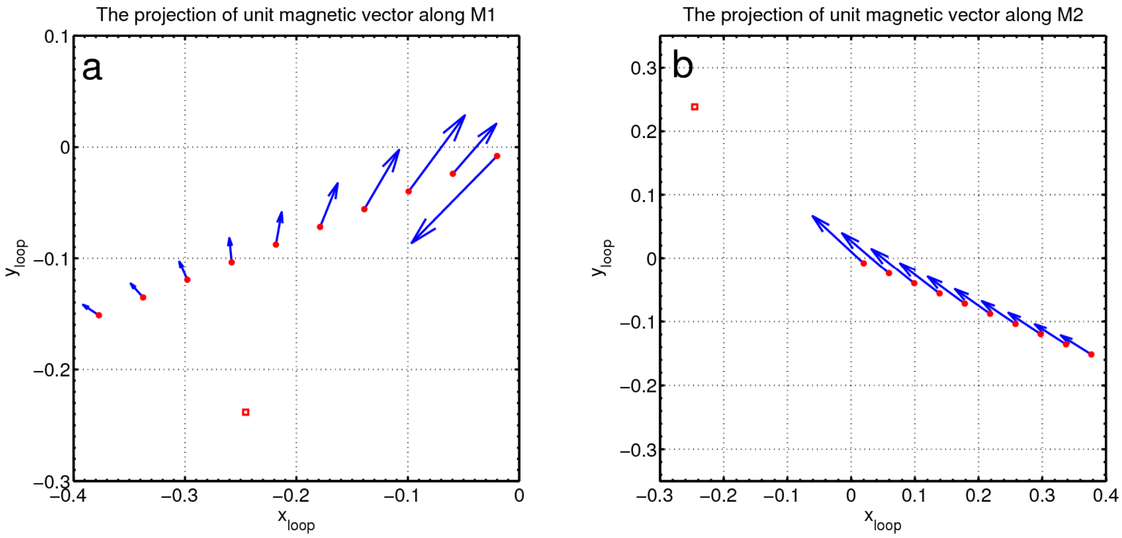

Figure S3. The projection of magnetic field direction on the equatorial plane of loop coordinates. The red dots represent the location of spacecraft with $z_i^{'} > 0$, the blue arrows are the projected directions of sampled field vectors, and the red square represents the loop center.

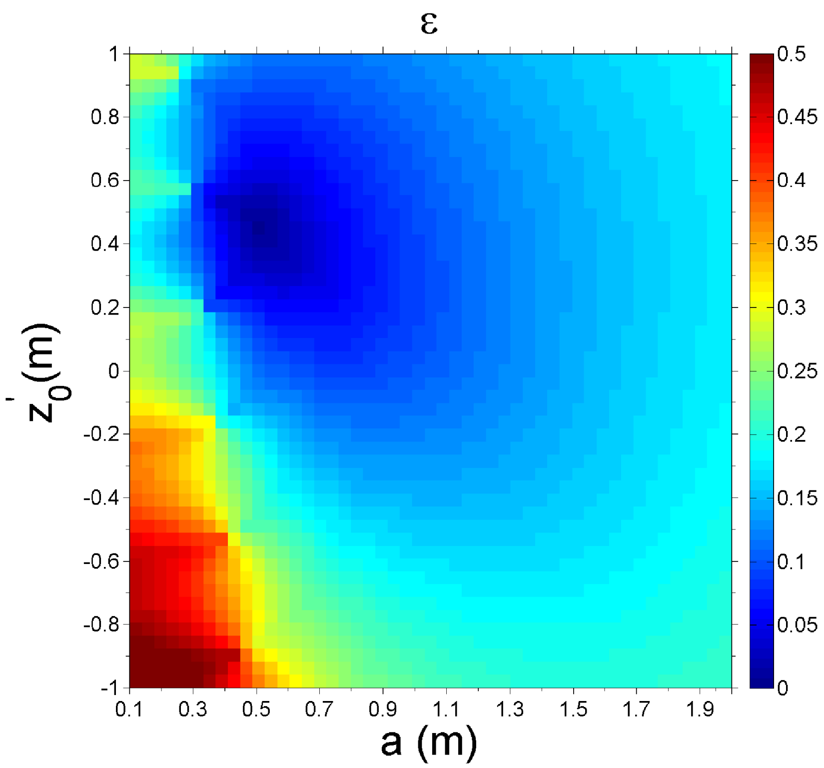

Figure S4. The 2-D distribution of ε

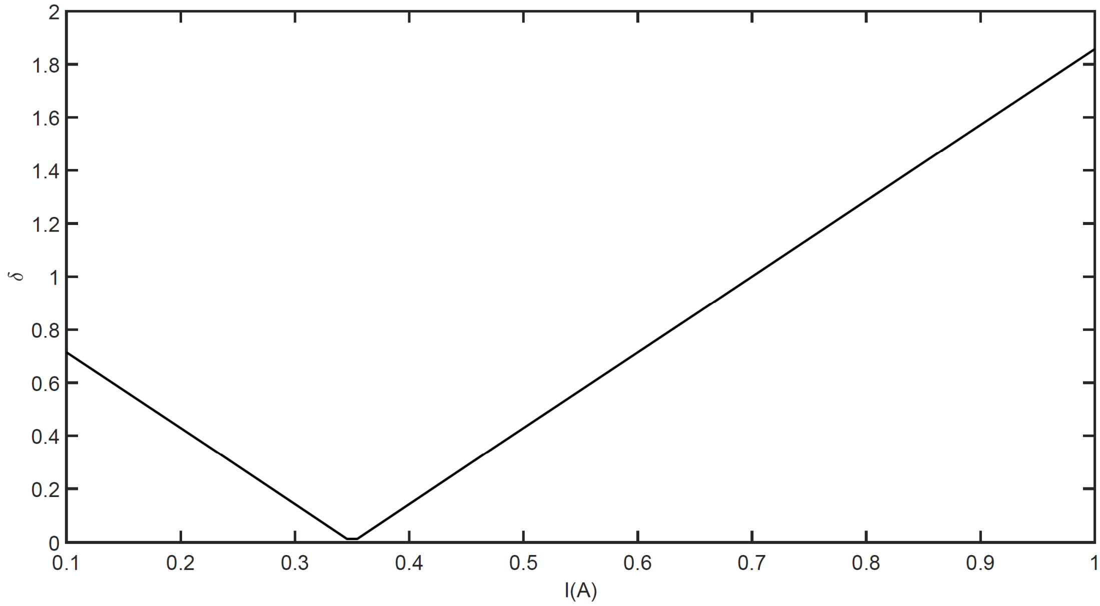

Figure S5. The variation of δ against I.

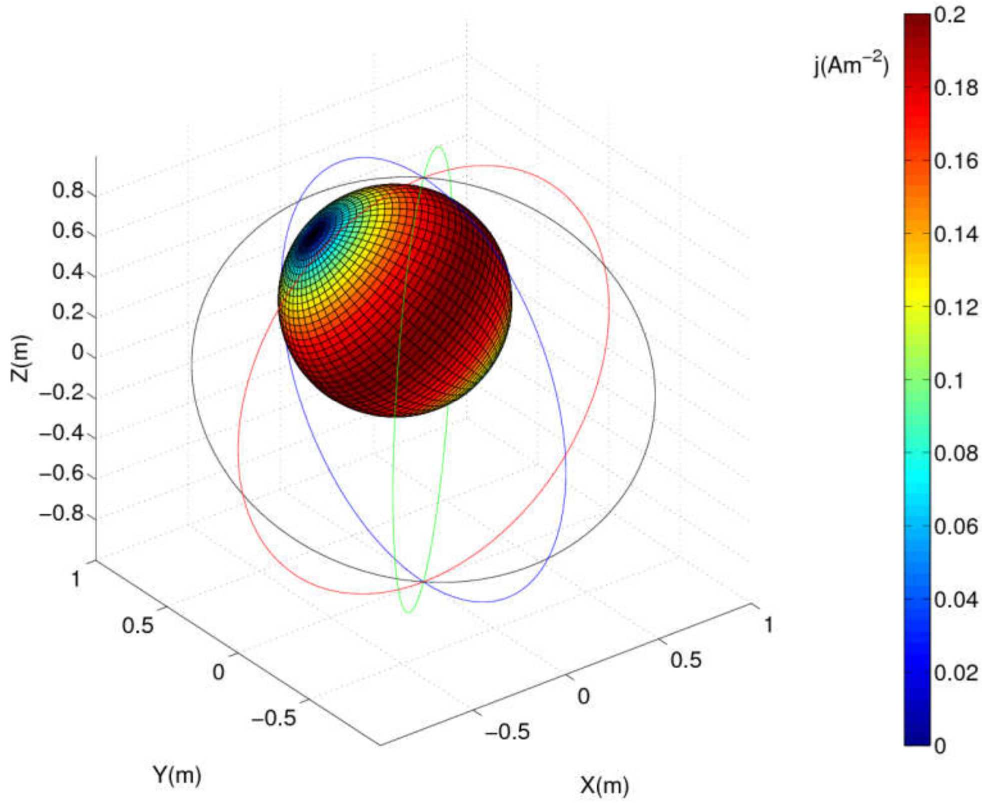

Figure S6. Test with four orbits on the magnetic field whose source is the current on a spherical surface. The distribution of surface current density j=0.2*$sin\theta$ is colored.

Table S1. The inversed single loop parameters when magnetic source is the current flowing on a spherical surface.

Models	x_0 (m)	y_0 (m)	z_0 (m)	a (m)	I (A)	M (Am2)	θ_0 (°)	φ_0 (°)	$\alpha_{\min}$ (°)	ε (°)	δ
$j_0*cos^2\theta$	~	~	~	~	~	~	45	150	0	~	~
$j_0*(cos^2\theta)^{1/2}$	~	~	~	~	~	~	45	150	0	~	~
j_0	~	~	~	~	~	~	45	150	0	~	~
$j_0*sin\theta$	~	~	~	~	~	~	45	150	0	~	~
$j_0*sin^2\theta$	-0.0002	0.2001	0.3002	0.1980	0.7522	0.0926	45	150	0	0.1310	0.0040
$j_0*sin^5\theta$	-0.0004	0.2003	0.3005	0.3245	0.2177	0.0720	45	150	0	0.3438	0.0101
$j_0*sin^{10}\theta$	-0.0006	0.2003	0.3006	0.3919	0.1157	0.0558	45	150	0	0.4229	0.0123
$j_0*sin^{20}\theta$	-0.0004	0.2002	0.3005	0.4389	0.0687	0.0416	45	150	0	0.3741	0.0111
$j_0*sin^{50}\theta$	-0.0002	0.2001	0.3002	0.4743	0.0385	0.0272	45	150	0	0.2290	0.0069

Table S2. The geomagnetic field data of global geomagnetic observatories recorded on 2015-01-01 00:00:00. The columns from left to the right show the IAGA name of observatories, the latitude and longitude of observatories, the northward (X), the eastward (Y), the downward (Z) component, and the field strength (F) of geomagnetic field in the local geographic coordinates, respectively. The unavailable data is assigned as 99999. The field data can be also accessible at the website http://www.intermagnet.org/index-eng.php

IAGA code	Latitude(Deg.)	Longitude(Deg.)	X(nT)	Y(nT)	Z(nT)	F(nT)
AAA	43.2	73.9	24668.5	2177.4	49102.2	54993.05
AAE	9.03	38.7	36252.54	1240.1	1954.29	36326.32
ABG	18.62	72.87	38119.1	140.1	19810.8	42960
ABK	68.358	18.823	11335.7	1617.8	51892.1	53140.63
AIA	-65.25	295.75	19954.7	5694.2	-32135.8	99999
AMS	-37.8	77.57	13805.42	-11710	-49494.34	52697.46
API	-13.8	188.22	32655	6915.6	-20051	38938.23
ARS	56.433	58.567	15650.6	3709.3	53880.1	56229.18
ASC	-7.95	345.62	19931.6	-5472	-19684.1	28542.21
ASP	-23.77	133.88	30086	2477.8	-43767.5	53168.61
BDV	49.08	14.02	20382.5	1201.2	44139.2	48632.69
BEL	51.84	20.79	18922.5	1902.3	46474.3	50214.84
BFO	48.331	8.325	20943.6	677.3	43306.1	48109.37
BLC	64.318	263.988	6707	-369.4	58424.6	58809.48
BMT	40.3	116.2	28024.1	-3868.1	47270.5	55088.83
BOU	40.14	254.76	20550.2	3183.4	48047.5	52354.62
BOX	58.07	38.23	15257.3	3235.8	50272	52635.92
BRD	49.87	260.0261	15038.3	1420.3	55142	57173.39

BRW	71.34	203.38	8704	2444.3	56745.3	57460.77
BSL	30.35	270.36	23936.6	-325	41303.7	47739.52
CKI	12.1875	96.8336	34568.1	-1405.4	-32752	47640.55
CLF	48.02	2.27	21182.9	61.6	42863.4	47812.03
CMO	64.87	212.14	11883.6	4023.5	55425.9	56827.95
CNB	35.32	149.36	23179.3	5135	-52954.3	58032.5
CSY	66.283	110.533	-979.1	-9134.7	-63394.6	64056.32
CTA	-20.1	146.3	31501.2	4092.2	-37470.4	49123.04
CYG	36.37	126.854	30083.6	-4088.4	40104.3	50299.93
CZT	-46.43	51.87	10455.1	-12388.9	-34451.3	38074.95
DED	70.36	211.21	8438.4	2931.1	56861.7	57558.41
DLT	11.94	108.48	40778.7	-458	8164.1	41590.64
DMC	-75.25	124.167	-8247.96	-6407.33	-61822.25	62702.75
DOU	50.1	4.6	20103.6	261.4	44184.9	99999
DRV	-66.67	140.01	-1868.96	169.21	-69110.94	69140.11
EBR	40.957	0.333	25189.8	18.7	37497.7	45173.14
ESK	55.32	356.8	17512.3	-834.1	46449.5	49648.29
EYR	-43.474	172.393	99999	99999	99999	99999
FCC	58.759	265.912	9400.2	-286.9	57838.6	58598.11
FRD	38.2	282.63	21012	-3920.5	46700.2	51359.35
FRN	37.09	240.28	22772.5	5304.4	42388.9	48410.14
FUR	48.17	11.28	20951.4	982.2	43458.2	48254.66
GAN	0.6946	73.1537	37647.7	-2856.2	-13130.3	39974.49
GCK	44.6	20.8	22677.8	1713.6	42039.3	47796.87
GDH	69.252	306.467	7400.4	-4996.1	55745.6	99999
GNG	-31.356	115.715	23945.2	-712.1	-52701.6	57891.34
GUA	13.59	144.87	35784.3	687.9	7943.1	36661.62
GUI	28.32	343.57	27540.5	-3705	22732	35901.85
HAD	51	355.52	19709.7	-817	44330.4	48521.48
HBK	-25.88	27.71	12360.2	-3997.4	-25171.8	28325.29
HER	-34.43	19.23	9569.2	-4581.8	-23325.3	25624.83
HLP	54.61	18.82	17505.7	1436.1	47141.7	50306.77
HON	21.32	202	26997.3	4645.8	21217	34649.66
HRB	47.86	18.19	20986.3	1554.2	43795.2	99999
HRN	77	15.37	7821.1	1002.5	53989.7	99999
HUA	-12.05	284.67	24974.2	-1143.6	-106	99999
HYB	17.4	78.6	39421.5	-516.9	17637.6	43190.25
IPM	-27.2	250.58	25046.2	7052.7	-19454.9	32489.57
IQA	63.753	291.482	8260.1	-4241.1	56300	57060.45
IRT	52.27	104.45	18554.6	-1127.4	57411.9	99999
IZN	40.5	29.72	25063.1	2232.3	40205.6	47430.39
JAI	26.92	75.8	35233.2	35.6	31190.1	99999
JCO	70.356	211.201	8451.4	2954.2	56862	57561.79
KAK	36.23	140.18	29709.5	-3827.8	35694.1	46598.02
KDU	-12.69	132.47	35421.7	1972.5	-29611.6	46210.76
KEP	-54.282	323.5071	15630.5	-1968.4	-23076.7	27941.29

KHB	47.61	134.69	23334	-5251.5	49170.3	99999
KIV	50.72	30.3	19170.7	2545.9	46676.3	99999
KMH	-26.54	18.11	99999	99999	99999	99999
KNY	31.42	130.88	32475.8	-3662	33146.3	46548.52
KOU	5.21	307.27	26564.8	-8593.8	7606.4	28937.75
LER	60.13	358.82	15018.5	-505.9	48610.8	50880.46
LON	45.4081	16.6592	22343.9	1460.8	42199.7	99999
LRM	-22.22	114.1	30128	156.4	-43457.9	52879.75
LVV	49.9	23.75	19907.8	2113.1	45628	99999
LYC	64.6	18.8	13016.5	1539.8	50573.1	52243.93
LZH	36.1	103.84	30550.9	-1228.2	43962.5	53549.87
MAB	50.298	5.682	19972.2	377	44444.2	99999
MAW	-67.6	62.88	6918.8	-17189.4	-45572.9	49196.27
MBO	14.38	343.03	32193.1	-4218.1	4072.6	32722.88
MCQ	-54.5	158.95	10756	6701.9	-62844.8	64109.48
MEA	54.616	246.653	13509.2	3607.2	55739.9	57466.92
MGD	60.051	150.728	16797.6	-3995.4	53468	56186.54
MMB	43.91	144.19	25801.7	-4016.1	42401.5	49797.03
NAQ	61.16	314.558	11844.1	-5087.9	52878.4	99999
NCK	47.63	16.72	21120	1448.5	43529.3	99999
NEW	48.27	242.88	17465.2	4788	51731.1	54809.35
NGK	52.07	12.68	18853	1054	45560.5	49318.41
NUR	60.51	24.66	14815.3	2054.7	50050.1	99999
NVS	54.85	83.23	16208	2358.1	57418.5	59709.03
ORC	-60.737	315.26	17817.8	-304.27	-26857.2	32484.9
OTT	45.4003	284.448	17703.2	-4353.3	51384.4	54522.88
PAF	-49.35	70.26	10094.95	-14707.92	-45849.94	49198.65
PAG	42.5	24.2	23692.8	1804.8	40799	47213.83
PEG	38.1	23.9	26416	1987.4	37500.8	45916.1
PET	52.971	158.248	21491.9	-2282.2	47153.5	51870.84
PHU	21.03	105.95	38825	-960.7	23103.6	45189.48
PPT	-17.57	210.42	29268.5	5877.5	-19094.9	35436.95
PST	-51.7	302.11	18341.3	964.2	-21702	28430.79
RES	74.69	265.105	2409.2	-1079.3	57614.3	57674.65
SBA	-77.85	166.78	99999	99999	99999	99999
SBL	43.9321	299.9905	19745.5	-6350.9	46362	50789.99
SFS	36.667	354.055	27509.3	-801.5	33020.9	42985.86
SHU	55.35	199.54	19407.8	3928.3	48428	52320.24
SIT	57.06	224.67	14876.5	5275	53497	55776.82
SJG	18.11	293.85	26302.6	-5978.9	25642.4	37217.12
SOD	67.37	26.63	11302.4	2255.5	51560.7	52833.21
SON	25.1168	66.4487	34794.98	419.15	27940.2	44626.3
SPG	60.542	29.716	14542.3	2548.3	50257	52381.11
SPT	39.55	355.65	25994.4	-560.7	35894.6	44322.17
STJ	47.595	307.323	18799.1	-6286.3	47138.2	51136.42
SUA	44.68	26.25	22590.4	2086.4	42662.6	48319.23

TAM	22.79	5.53	33686.3	6.7	17095.3	37775.97
TDC	-37.067	347.685	9461.3	-3793.6	-22426.8	24635.01
THL	77.47	290.773	2734.2	-3087.2	56189.7	99999
THY	46.9	17.89	21495.1	1533.4	43213.1	48288.33
TRW	-43.3	294.7	19655.84	1734.3	-17790.3	26567.7
TSU	-19.202	17.584	14052.7	-2288.8	-25835.5	99999
TUC	32.18	249.27	24052.2	3988.2	40782.5	47514.29
UPS	59.903	17.353	15130.4	1430	49050.8	51351.29
VAL	51.933	349.75	19379.5	-1664.3	44733.1	99999
VIC	48.52	236.58	18081.6	5374.9	50457.8	53867.68
VNA	-70.683	351.718	99999	99999	99999	99999
VOS	-78.464	106.835	-7519.2	-11337.8	-57798	99999
VSS	-22.4	316.35	16896.58	-6989.06	-14428.1	23290.67
WIC	47.9305	15.8657	20989.4	1377	43659.1	48461.93
WNG	53.74	9.07	18158	713.1	46133.6	49583.27
YAK	61.96	129.66	13457	-4944.6	58145.1	59882.7
YKC	62.48	245.518	8800.7	2715.9	57798.2	58527.63